Composite Structures 252 (2020) 112677

Contents lists available at ScienceDirect

Composite Structures

journal homepage: www.elsevier.com/locate/compstruct

Surrogate based optimization of functionally graded plates using radial basis functions

Leonardo Gonçalves Ribeiro, Marina Alves Maia, Evandro Parente Jr. *, Antônio Macário Cartaxo de Melo

Laboratório de Mecânica Computacional e Visualização, Departamento de Engenharia Estrutural e Construção Civil, Universidade Federal do Ceará, Fortaleza CE, Brazil

ARTICLE INFO

Keywords:
Functionally graded plates
Sequential approximate optimization
Radial basis functions
Surrogate modeling

ABSTRACT

This work presents an efficient methodology for optimum design of functionally graded plates. Isogeometric analysis is used to evaluate the structural responses and the material gradation is described using B-Splines to enhance design flexibility. A constraint is included in the optimization model to ensure a smooth material gradation. In order to improve the computational efficiency of the optimization process, a surrogate model based on Radial Basis Functions is used to accurately approximate the structural responses. Different methods to define the width of basis functions based on analytical and cross-validation techniques are adopted and compared. Two infill criteria based on the expected improvement technique are used to continuously improve the surrogate model accuracy by balancing both the local and global searches. The accuracy and efficiency of the proposed approaches are assessed through a set of problems involving the maximization of the buckling load and the fundamental frequency of functionally graded plates, showing excellent results.

1. Introduction

Functionally Graded Materials (FGM) are a class of advanced composites with a gradual and continuously varying composition. This feature allows the mechanical properties of a structure to vary smoothly, eliminating interface problems often seen in laminated composites due to interlaminar stress discontinuity. Initially developed in Japan in the mid-1980s, the FGM were proposed to be used as a thermal barrier for the aerospace industry by taking advantage of properties such as the good thermal resistance of ceramic materials and the high mechanical resistance of metallic materials [1].

Once the materials are chosen, the design of functionally graded structures requires the definition of the material gradation. Since this is a complex problem, to fully explore the potential of FGMs requires the use of optimization techniques. Kou et al. [2] proposed a model where properties may change over all reference axes. By treating the gradation as the design variable, the authors used the Particle Swarm Optimization (PSO) to minimize the thermal stresses of different structures. It was shown that heuristic approaches outperform mathematical programming methods in these problems due to their global search capabilities.

Ashjari and Khoshravan [3] performed the mass minimization of unidirectional functionally graded plates subjected to deflection and stress constraints. Hermite-polynomials with equally spaced control points were used to model the volume fraction variation along the plate thickness. They showed that the PSO outperforms the Genetic Algorithm in these problems both in terms of convergence speed and accuracy.

Shi and Shimoda [4] showed that the compliance of functionally graded sandwich structures can be reduced significantly by performing an interface shape optimization. Also regarding the design of sandwich structures, Loja et al. [5] used PSO to maximize the bending stiffness of unidirectional FG beams considering a mass constraint. This objective function was chosen to reduce the computational cost avoiding the need of carry out finite element analysis.

Kim et al. [6] used a Differential Evolution (DE) algorithm to maximize the first three natural frequencies of FG beams. The authors point out that the FG performance is dependent on the design flexibility. Thus, material gradation is defined by a two-dimensional NURBS surface and Isogeometric Analysis (IGA) is used to assess the structural response. A similar approach is also applied by Truong et al. [7] to minimize the compliance of a Timoshenko beam under static load.

Correia et al. [8] performed a multi-objective optimization of FG plates subjected to buckling and vibration constraints. The Finite Element Method (FEM) was used for structural analysis and a mathematical programming technique was used for optimization. Four objective functions were considered: the maximization of the first natural frequency and the buckling load parameter and the minimization of the overall mass and material costs. The material gradation was defined using a power-law function. Results showed that considerable saving

* Corresponding author.

https://doi.org/10.1016/j.compstruct.2020.112677
Received 31 March 2020; Revised 30 May 2020; Accepted 29 June 2020
Available online 15 July 2020

on the mass and the cost of the plates can be achieved whilst improving the structural behavior. A similar methodology was presented by Correia et al. [9] with the consideration of thermo-mechanical loading.

Lieu et al. [10] used the Adaptive Hybrid Evolutionary Firefly Algorithm (AHEFA) to perform the maximization of the fundamental frequency of sandwich FG plates. The material gradation through the plate thickness is defined using B-Splines. Later, Lieu and Lee [11] attested the performance of AHEFA for the optimization of bi-directional FG plates. In this work, the thickness also varies according to a B-Spline function, increasing the design flexibility. This framework was later adapted to the Reliability Based Design Optimization (RBDO) of FG plates [12].

Wang et al. [13] used a modified PSO in order to carry out the multi-objective optimization of FG plates. The mass and the first natural frequency were taken as objective functions and a volume constraint was considered. IGA was used to evaluate the structural behavior and B-Splines were used to define the material gradation over the plate thickness. The use of B-Splines increase the design flexibility with respect to the use of a power-law.

The effectiveness of numerical methods, as FEM and IGA, is well known in the analysis of FG structures, such as beams and plates [14,13,15]. However, an optimization process entailing their use may quickly become impractical due to a high computational cost. A common approach to speed up the procedure is the parallelization of the optimization process by taking advantage of multiple cores machines [16,17]. Although this approach is capable of achieving excellent results, parallel computing resources are not always available.

An alternative approach is to use surrogate models to approximate the structural responses at a much lower cost than directly using computational methods for structural analysis. These approximate models are built using the high fidelity structural responses evaluated at chosen sampling points distributed over the design space [18]. Polynomial Regression (PR), Artificial Neural Network (ANN), Radial Basis Functions (RBF), Support Vector Regression (SVR), and Kriging are some of the most popular surrogate models [19,18,20,21].

Although the surrogate modelling technique has already been applied in many areas of structural engineering [22,23,18,24–31], few papers have focused on their application over FG structures. Chen et al. [32] presented a parameter optimization for Multiquadric Radial Basis Functions for estimating the deflection and the stress on FG plates. Cheng et al. [33] used a Kriging model in the optimization process of a dental implant considering dynamic loads. Truong et al. [34] adopted an ANN to speed up the optimization of FG beams, showing that the approach greatly reduces computational cost while still being able to find optimal designs, either maximizing the fundamental frequency or minimizing the weight. Do et al. [15] used a Deep Neural Network (DNN) in the optimization of FG plates. Isogeometric Analysis (IGA) was used to evaluate the structural behavior and B-Splines were used to define the material gradation over the plate thickness. The buckling load and the first natural frequency were taken as objective functions and a volume constraint was considered.

These works considered a fixed surrogate model during the design optimization. However, this approach may demand a high number of sampling points to achieve good accuracy over the entire design space due to the lack of definition of regions of interest. Therefore, the use of a Sequential Approximate Optimization (SAO) is more efficient since the model is updated with new sampling points only in the promising regions of the design space.

This work presents a surrogate based methodology for the optimization of FG plates. A NURBS-based isogeometric formulation is used as high fidelity model for structural analysis. B-Splines are used to define the material gradation over the plate thickness in order to improve the design flexibility. The buckling load and the first natural frequency are considered as objective functions. The optimization model considers constraints regarding the volume fraction distribution and the total mass of the structure.

Radial Basis Functions are used as a surrogate model to improve the efficiency of the optimization process. This surrogate model was chosen due to its simplicity [35] and accuracy for higher-dimensional and non-linear functions [36–38]. One key aspect in the accuracy and efficiency of RBF models is the definition of the width of the basis functions. Therefore, two analytic and two cross-validation methods are compared in terms of both accuracy and efficiency. In order to lower the computational cost of the surrogate based optimization, two different Sequential Approximate Optimization approaches are used to update the surrogate model using the Expected Improvement as infill criterion. The performance of these SAO approaches are compared using optimization problems of FG plates.

The rest of the paper is organized as follows. Section 2 addresses characterization and analysis of FG plates. Section 3 presents the Particle Swarm Optimization algorithm used to find the best infill points and to optimize the objective function. Section 4 discusses the surrogate based optimization, including the Design of Experiments and the evaluation of RBF parameters. Section 5 presents the Sequential Approximate Optimization procedure, including the Expected Improvement technique. The numerical examples are presented in Section 6 and the conclusions are discussed in Section 7.

2. Functionally graded plates

This study considers Functionally Graded (FG) plates made of two materials whose proportion varies smoothly across the thickness, as depicted in Fig. 1.

The definition of the effective material properties is of utmost importance for analysis and design of functionally graded structures, and it depends on the properties of the constituents and proportion of each material at each point. These properties are evaluated using homogenization techniques discussed in the following.

The design optimization of FGPs consists mainly on the definition of the material gradation that results in the best structural performance. For a high design flexibility, the material gradation is often described by B-Splines [39,10,15,13].

Considering a FG structure with two different materials, e.g. a metal (m) and a ceramic (c), the volume fraction variation is defined as:

$$V_c(\xi) = \sum_{i=1}^{n_{cp}} B_{i,p}(\xi)\, V_{c,i}, \quad \xi \in [0,1] \tag{1}$$

$$V_c(\xi) + V_m(\xi) = 1 \tag{2}$$

where n_{cp} is the number of control points, $V_{c,i}(z)$ is the ceramic volume fraction of the i-th control point, $B_{i,p}$ is the corresponding B-Spline basis, p is the basis degree, and ξ is the parametric coordinate. The definition of $B_{i,p}$ basis requires a knot vector, composed by non-negative and non-decreasing parametric values bounded by the parametric interval in

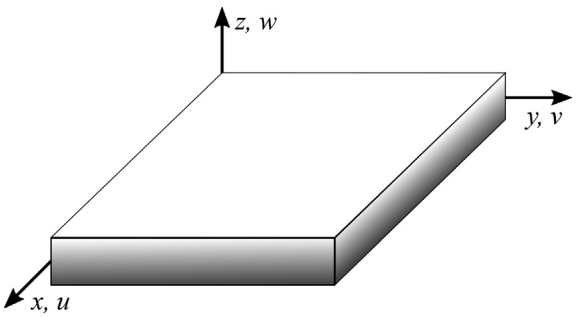

Fig. 1. Functionally graded plate.

which the B-Spline is defined. Given a knot vector $\Xi = [\xi_1, \xi_2, \ldots, \xi_{n+p+1}]$, the B-Spline basis functions are evaluated by the recursive Cox-de Boor formula [39]:

$$B_{i,p}(\xi) = \frac{\xi - \xi_i}{\xi_{i+p} - \xi_i} B_{i,p-1}(\xi) + \frac{\xi_{i+p+1} - \xi}{\xi_{i+p+1} - \xi_{i+1}} B_{i+1,p-1}(\xi) \tag{3}$$

$$B_{i,0}(\xi) = \begin{cases} 1, & \xi_i \leqslant \xi < \xi_{i+1} \\ 0, & \text{otherwise} \end{cases} \tag{4}$$

The smoothness of the B-Spline depends on the knot vector, since the basis $B_{i,p}$ has continuity C^{p-k} at the knots, where k is the knot multiplicity [39]. Open knot vectors with equally spaced interior knots will be used in this work to ensure a smooth material gradation.

2.1. Effective material properties

The evaluation of effective material properties requires the use of an appropriate homogenization scheme [40,1,41]. The simplest and most used approach is the Voigt model, also known as the Rule of Mixtures (RoM), where the effective material property (P) is given by the weighted average of the constituents properties:

$$P = P_m V_m + P_c V_c \tag{5}$$

The Voigt model gives good results for the specific mass (ρ), but poor results for other mechanical properties. Therefore, the elastic properties will be computed in this work using the Mori-Tanaka model [40,1,41]. Considering a matrix with spherical inclusions, the bulk modulus (K) and the shear modulus (G) are given by [42,43]:

$$\begin{aligned} \frac{K-K_m}{K_c-K_m} &= \frac{V_c}{1+\dfrac{3\,V_m\,(K_c-K_m)}{3K_m+4\,G_m}} \\ \frac{G-G_m}{G_c-G_m} &= \frac{V_c}{1+\frac{V_m\,(G_c-G_m)}{G_m+f_m}} \end{aligned} \tag{6}$$

where the parameter f_m is given by:

$$f_m = \frac{G_m(9K_m - 8G_m)}{6(K_m + 2G_m)} \tag{7}$$

After that, the effective Young's modulus (E) and Poisson's ratio (ν) are computed according to standard expressions [1].

2.2. Governing equations

According to the Reissner-Mindlin theory, also known as the First-order Shear Deformation Theory (FSDT), the displacements of the plate, at any point, can be written in matrix form as [44–46]:

$$\begin{bmatrix} \overline{u} \\ \overline{v} \\ \overline{w} \end{bmatrix} = \begin{bmatrix} 1 & 0 & 0 & 0 & z \\ 0 & 1 & 0 & -z & 0 \\ 0 & 0 & 1 & 0 & 0 \end{bmatrix} \begin{bmatrix} u \\ v \\ w \\ \theta_x \\ \theta_y \end{bmatrix} \Rightarrow \overline{\mathbf{u}} = \mathbf{Z}\,\mathbf{u} \tag{8}$$

where u, v and w are the midsurface displacements in the x, y and z directions; θ_x and θ_y are the rotations about x and y axes, respectively; z is the distance from a point to the midsurface.

Using the von Kármán theory, the in-plane strains can be written as

$$\boldsymbol{\varepsilon} = \begin{bmatrix} \varepsilon_x \\ \varepsilon_y \\ \gamma_{xy} \end{bmatrix} = \boldsymbol{\varepsilon}^m + z\boldsymbol{\kappa} \tag{9}$$

where the membrane strains ($\boldsymbol{\varepsilon}^m$) and curvatures ($\boldsymbol{\kappa}$) are given by

$$\boldsymbol{\varepsilon}^m = \begin{bmatrix} u_{,x} \\ v_{,y} \\ u_{,y} + v_{,x} \end{bmatrix} + \begin{bmatrix} \frac{1}{2}w_{,x}^2 \\ \frac{1}{2}w_{,y}^2 \\ w_{,x}\,w_{,y} \end{bmatrix}, \quad \boldsymbol{\kappa} = \begin{bmatrix} \theta_{y,x} \\ -\theta_{x,y} \\ \theta_{y,y} - \theta_{x,x} \end{bmatrix} \tag{10}$$

Furthermore, the transverse shear strains are:

$$\boldsymbol{\gamma} = \begin{bmatrix} \gamma_{xz} \\ \gamma_{yz} \end{bmatrix} = \begin{bmatrix} w_{,x} + \theta_y \\ w_{,y} - \theta_x \end{bmatrix} \tag{11}$$

Assuming an elastic isotropic behavior, the constitutive relation for in-plane stresses ($\boldsymbol{\sigma}$) and strains ($\boldsymbol{\varepsilon}$) is given by

$$\begin{bmatrix} \sigma_x \\ \sigma_y \\ \tau_{xy} \end{bmatrix} = \begin{bmatrix} Q_{11} & Q_{12} & 0 \\ Q_{12} & Q_{22} & 0 \\ 0 & 0 & Q_{66} \end{bmatrix} \begin{bmatrix} \varepsilon_x \\ \varepsilon_y \\ \gamma_{xy} \end{bmatrix} \Rightarrow \boldsymbol{\sigma} = \mathbf{Q}\boldsymbol{\varepsilon} \tag{12}$$

where

$$Q_{11} = Q_{22} = \frac{E}{1-\nu^2};\; Q_{12} = \nu Q_{11};\; Q_{66} = \frac{E}{2(1+\nu)} \tag{13}$$

In addition, the transverse shear stresses ($\boldsymbol{\tau}$) are computed from

$$\begin{bmatrix} \tau_{xz} \\ \tau_{yz} \end{bmatrix} = \begin{bmatrix} Q_{44} & 0 \\ 0 & Q_{55} \end{bmatrix} \begin{bmatrix} \gamma_{xz} \\ \gamma_{yz} \end{bmatrix} \Rightarrow \boldsymbol{\tau} = \mathbf{Q}_s\boldsymbol{\gamma} \tag{14}$$

where $Q_{44} = Q_{55} = Q_{66}$.

The internal forces and moments are obtained integrating stresses through the plate thickness as presented in Praciano et al. [45]. Finally, the stress resultants $\hat{\boldsymbol{\sigma}}$ can be written in terms of the generalized strains $\hat{\boldsymbol{\varepsilon}}$ as:

$$\begin{bmatrix} \mathbf{N} \\ \mathbf{M} \\ \mathbf{V} \end{bmatrix} = \begin{bmatrix} \mathbf{A} & \mathbf{B} & \mathbf{0} \\ \mathbf{B} & \mathbf{D} & \mathbf{0} \\ \mathbf{0} & \mathbf{0} & \mathbf{G} \end{bmatrix} \begin{bmatrix} \boldsymbol{\varepsilon}^m \\ \boldsymbol{\kappa} \\ \boldsymbol{\gamma} \end{bmatrix} \Rightarrow \hat{\boldsymbol{\sigma}} = \mathbf{C}\hat{\boldsymbol{\varepsilon}} \tag{15}$$

where $\mathbf{A}, \mathbf{B}, \mathbf{D}$ and $\mathbf{G}$ are the extensional, membrane-bending coupling, bending and shear stiffness matrices, respectively, whose elements are given by:

$$\begin{aligned} [A_{ij}, B_{ij}, D_{ij}] &= \int_{-h/2}^{h/2} Q_{ij}(z)[1, z, z^2]\,dz \\ G_{ij} &= k_s \int_{-h/2}^{h/2} Q_{s_{ij}}(z)\,dz \end{aligned} \tag{16}$$

where k_s is the shear correction factor (taken as 5/6 in this work). It is important to note that a symmetric material distribution through thickness results in $\mathbf{B} = \mathbf{0}$. On the other hand, non-symmetric volume fraction variations lead to bending-membrane coupling.

The dynamic equilibrium equations of the model can be obtained using the D'Alembert and virtual work principles:

$$\int_A \delta\mathbf{u}^T \overline{\mathbf{M}}\,\ddot{\mathbf{u}}\,dA + \int_A \delta\hat{\boldsymbol{\varepsilon}}^T\hat{\boldsymbol{\sigma}}\,dA = \int_A \delta\mathbf{u}^T\mathbf{q}\,dA + \int_S \delta\mathbf{u}^T\mathbf{f}_s\,dS \tag{17}$$

where $\mathbf{q}$ is the surface load, $\mathbf{f}_s$ is the boundary load, A and S are the midsurface area and midsurface boundary of the plate, respectively, and $\overline{\mathbf{M}}$ is obtained using Eq. (8) as in:

$$\overline{\mathbf{M}} = \int_{-h/2}^{h/2} \rho\mathbf{Z}^T\mathbf{Z}\,dz = \begin{bmatrix} I_0 & 0 & 0 & 0 & I_1 \\ 0 & I_0 & 0 & -I_1 & 0 \\ 0 & 0 & I_0 & 0 & 0 \\ 0 & -I_1 & 0 & I_2 & 0 \\ I_1 & 0 & 0 & 0 & I_2 \end{bmatrix} \tag{18}$$

and

$$[I_0, I_1, I_2] = \int_{-h/2}^{h/2} \rho(z)\left[1, z, z^2\right] dz \tag{19}$$

In this work, Gaussian quadrature is used to carry-out the integrations presented in Eq. (16) and (19).

2.3. Isogeometric analysis

NURBS are widely used in geometric modeling since they offer a mathematical description capable to represent both analytic (e.g. cir-

cles and ellipses) and free-form curves and surfaces using the same database.

A tensor product NURBS surface (S) of degree ($p \times q$) is defined by a linear combination of bivariate rational basis functions (R) and a matrix of control points ($\mathbf{p}$):

$$S(\xi,\eta) = \sum_{i=1}^{n}\sum_{j=1}^{m} R_{ij}(\xi,\eta)\, p_{ij} \tag{20}$$

where ξ and η are the parametric coordinates. The rational basis functions R are evaluated based on a set of weights w_{ij} associated to each control point and B-Spline basis functions B defined for each parametric variable:

$$R_{ij}(\xi,\eta) = \frac{B_{i,p}(\xi)\, B_{j,q}(\eta)\, w_{ij}}{W(\xi,\eta)} \tag{21}$$

where W is the bivariate weight function expressed as:

$$W(\xi,\eta) = \sum_{i=1}^{n}\sum_{j=1}^{m} B_{i,p}(\xi)\, B_{j,q}(\eta)\, w_{ij} \tag{22}$$

In the isogeometric formulation used in this work, the plate geometry is described by a bivariate NURBS:

$$x = \sum_{k=1}^{n_{cp}} R_k\, x_k, \quad y = \sum_{k=1}^{n_{cp}} R_k\, y_k \tag{23}$$

where R_k are the functions defined by Eq. (21) and n_{cp} is the number of control points of the surface. Furthermore, the in-plane and transverse displacements and rotations at the plate mid-surface are approximated from the element degrees of freedom at control points as:

$$\begin{aligned} &u = \sum_{k=1}^{n_{cp}} R_k\, u_k, \quad v = \sum_{k=1}^{n_{cp}} R_k\, v_k, \quad w = \sum_{k=1}^{n_{cp}} R_k\, w_k \\ &\theta_x = \sum_{k=1}^{n_{cp}} R_k\, \theta_{xk}, \quad \theta_y = \sum_{k=1}^{n_{cp}} R_k\, \theta_{yk} \end{aligned} \tag{24}$$

This equation can be written in matrix format as

$$\mathbf{u} = \mathbf{R}\,\mathbf{d} \tag{25}$$

where $\mathbf{d}$ is the vector of degrees of freedom, corresponding to the displacements at control points, and $\mathbf{R}$ is the matrix of shape functions:

$$\mathbf{R} = [\,\mathbf{R}_1 \quad \mathbf{R}_2 \quad \ldots \quad \mathbf{R}_{nc}\,] \tag{26}$$

where

$$\mathbf{R}_k = R_k\, \mathbf{I}_{5x5} \tag{27}$$

The generalized strains are related to the degrees of freedom:

$$\hat{\boldsymbol{\varepsilon}} = \begin{bmatrix} \varepsilon_0^m + \varepsilon_L^m \\ \kappa \\ \gamma \end{bmatrix} = \begin{bmatrix} \mathbf{B}_0^m \\ \mathbf{B}_0^b \\ \mathbf{B}_0^s \end{bmatrix} \mathbf{d} + \frac{1}{2} \begin{bmatrix} \mathbf{B}_L^m \\ 0 \\ 0 \end{bmatrix} \mathbf{d} = \left(\mathbf{B}_0 + \frac{1}{2}\mathbf{B}_L\right)\mathbf{d} \tag{28}$$

Using Eqs. (10)–(11) and (24)–(27), the sub-matrices are defined by:

$$\begin{aligned} \mathbf{B}_0^m &= \begin{bmatrix} R_{k,x} & 0 & 0 & 0 & 0 \\ 0 & R_{k,y} & 0 & 0 & 0 \\ R_{k,y} & R_{k,x} & 0 & 0 & 0 \end{bmatrix} \\ \mathbf{B}_0^b &= \begin{bmatrix} 0 & 0 & 0 & 0 & R_{k,x} \\ 0 & 0 & 0 & -R_{k,y} & 0 \\ 0 & 0 & 0 & -R_{k,x} & R_{k,y} \end{bmatrix} \\ \mathbf{B}_0^s &= \begin{bmatrix} 0 & 0 & R_{k,x} & 0 & R_k \\ 0 & 0 & R_{k,y} & -R_k & 0 \end{bmatrix} \\ \mathbf{B}_L^m &= \begin{bmatrix} 0 & 0 & W_x R_{k,x} & 0 & 0 \\ 0 & 0 & W_y R_{k,y} & 0 & 0 \\ 0 & 0 & W_x R_{k,y} + W_y R_{k,x} & 0 & 0 \end{bmatrix} \end{aligned} \tag{29}$$

where:

$$W_x = \sum_{k=1}^{n_{cp}} R_{k,x}\, w_k, \quad W_y = \sum_{k=1}^{n_{cp}} R_{k,y}\, w_k \tag{30}$$

Substituting Eq. (24) in Eq. (17) and considering arbitrary virtual displacements, the dynamic equilibrium equations at a time t can be written as:

$$\mathbf{M}\ddot{\mathbf{d}} + \mathbf{g}(\mathbf{d}) = \mathbf{f}(t) \tag{31}$$

where

$$\mathbf{M} = \int_A \mathbf{R}^T\, \overline{\mathbf{M}}\, \mathbf{R}\, dA \tag{32}$$

$$\mathbf{f} = \int_A \mathbf{R}^T \mathbf{q}\, dA + \int_S \mathbf{R}^T \mathbf{f}_s\, dS \tag{33}$$

$$\mathbf{g} = \int_A \overline{\mathbf{B}}^T\, \hat{\boldsymbol{\sigma}}\, dA \tag{34}$$

$\mathbf{M}$ is the mass matrix and $\overline{\mathbf{B}} = \mathbf{B}_0 + \mathbf{B}_L$ is the matrix that relates the variation of the generalized strains with the variation of the control points displacements ($\delta\hat{\boldsymbol{\varepsilon}} = \overline{\mathbf{B}}\,\delta\mathbf{d}$).

The tangent stiffness matrix is obtained by differentiation of the internal force vector ($\mathbf{g}$):

$$\mathbf{K}_T = \frac{\partial \mathbf{g}}{\partial \mathbf{d}} = \mathbf{K}_L + \mathbf{K}_\sigma \tag{35}$$

where material stiffness matrix $\mathbf{K}_L$ and the geometric stiffness matrix $\mathbf{K}_\sigma$ are given by:

$$\mathbf{K}_L = \int_A \overline{\mathbf{B}}^T \frac{\partial \hat{\boldsymbol{\sigma}}}{\partial \mathbf{d}}\, dA = \int_A \overline{\mathbf{B}}^T\, \mathbf{C}\, \overline{\mathbf{B}}\, dA \tag{36}$$

$$\mathbf{K}_\sigma = \int_A \frac{\partial \overline{\mathbf{B}}^T}{\partial \mathbf{d}}\, \boldsymbol{\sigma}\, dA = \int_A \mathbf{G}^T\, \mathbf{S}\, \mathbf{G}\, dA \tag{37}$$

where $\mathbf{C}$ is the constitutive matrix defined in Eq. (17)

$$\mathbf{G} = \begin{bmatrix} 0 & 0 & R_{k,x} & 0 & 0 \\ 0 & 0 & R_{k,y} & 0 & 0 \end{bmatrix}, \quad \mathbf{S} = \begin{bmatrix} N_x & N_{xy} \\ N_{xy} & N_y \end{bmatrix} \tag{38}$$

The stiffness matrices are evaluated using an appropriate reduced integration scheme in order to avoid shear locking and improve the computation efficiency [45].

The free vibration analysis is carried-out solving the generalized eigenproblem:

$$\left(\mathbf{K} - \omega^2\, \mathbf{M}\right)\boldsymbol{\phi} = \mathbf{0} \tag{39}$$

where $\mathbf{K}$ is the stiffness matrix of the unloaded structure ($\mathbf{d} = \mathbf{0}$), ω are the natural frequencies, and $\boldsymbol{\phi}$ are the vibration modes.

For structures with negligible pre-buckling displacements, the stability analysis can be carried-out solving the generalized eigenproblem:

$$(\mathbf{K} + \lambda\, \mathbf{K}_\sigma)\boldsymbol{\phi} = \mathbf{0} \tag{40}$$

where $\mathbf{K}_\sigma$ is the geometric stiffness matrix due to the reference loads, λ are the buckling load factors, and $\boldsymbol{\phi}$ are the buckling modes.

3. Particle Swarm Optimization

The main goal of an optimization procedure is to find which vector of variables $\mathbf{x}$ minimizes a given objective function $f(\mathbf{x})$, while also respecting a set of constraints $g_i(\mathbf{x})$. Mathematically, one must find $\mathbf{x}$ that:

$$\begin{cases} \text{minimize } f(\mathbf{x}) \\ \text{subjected, to } g_i(\mathbf{x}) \leqslant 0, \quad i = 1, \ldots, n_c \\ \text{with } \mathbf{x}_L \leqslant \mathbf{x} \leqslant \mathbf{x}_U \end{cases} \tag{41}$$

where n_c is the number of constraints and $\mathbf{x}_L$ and $\mathbf{x}_U$ are the vectors containing the lower and upper bounds of each design variable. Maximization problems are easily handled by the minimization of $-f(\mathbf{x})$.

Since most optimization problems regarding functionally graded structures deal with continuous variables, this work uses the Particle Swarm Optimization (PSO) to find the global optimum in the design space. For these types of problems, previous researchers have already pointed out the better performance the PSO presents over mathematical programming [2], due to the existence of multiple local minima, and over the Genetic Algorithm [3] due to a faster convergence speed.

First introduced by Kennedy and Eberhart [47], PSO tries to mirror the behavior of a swarm such as a flock of birds or a school of fishes, replicating their continuous movement in search for better food supplies. Due to only requiring simple mathematical operators, the method itself is computationally inexpensive. A multitude of different versions of the algorithm is available, as many researchers tried to improve upon the original approach [48]. The version used in this work is presented in the following.

The algorithm is initialized by generating N_p particles, where each particle j is randomly assigned a position $\mathbf{x}_j^{(0)}$ and a velocity $\mathbf{v}_j^{(0)}$. At each iteration, the particles move through the design space based on their velocities such that the new position is given by:

$$\mathbf{x}_j^{(i+1)} = \mathbf{x}_j^{(i)} + \mathbf{v}_j^{(i+1)} \tag{42}$$

where $\mathbf{v}_j^{(i+1)}$ is defined by:

$$\mathbf{v}_j^{(i+1)} = w\mathbf{v}_j^{(i)} + c_1 r_1 \left(\mathbf{x}_{pj}^{(i)} - \mathbf{x}_j^{(i)}\right) + c_2 r_2 \left(\mathbf{x}_{gj}^{(i)} - \mathbf{x}_j^{(i)}\right) \tag{43}$$

where w is the inertia, c_1 is the cognitive factor, c_2 is the social factor, r_1 and r_2 are uniformly distributed random numbers between 0 and 1, $\mathbf{x}_{pj}^{(i)}$ is the best position the particle j obtained during the optimization and $\mathbf{x}_{gj}^{(i)}$ is the best position the particles on the neighborhood of particle j obtained during the optimization. Thus, both the cognitive and social experiences affect the particle velocity. The process continues until a stopping criteria is met. Two stopping criteria are used in this work: the maximum number of iterations (It_{max}) and the maximum number of iterations without improvement ($Stall_{max}$).

The neighborhood of a particle is defined according to a chosen topology, as illustrated in Fig. 2. The early PSO versions adopted the Global topology, where the particles are linked to the entire swarm. However, this approach may result in premature convergence to local minima. An alternative is to use the Square topology, where the swarm is arranged as a matrix and the particle has a neighbour in each direction (above, below, right and left), or the Ring topology, where each particle may only be influenced by the two closest ones. The use Square and Ring slow down the sharing of social experience between the particles improving the exploration of the design space and the global convergence of PSO [48,17].

PSO algorithms may often suffer from premature convergence for multimodal problems, even using Square or Ring topology, as the particles are attracted to the current best solution found by neighboring particles. In order to avoid this problem, a Mutation operator inspired by Genetic Algorithms, is considered in this work to maintain the swarm diversity [17]. This operator is applied to the particle position, where each variable has a small probability (p_{mut}) of mutating to a new random value, between the lower and upper bounds.

During the optimization process, a particle may violate a bound constraint leaving the design space. A simple procedure, illustrated in Fig. 3, is adopted in order to avoid this problem. When a particle leaves the search space, the variable that had its bounds violated is set to the bound. The velocity is modified to the opposite direction, which will affect the following iterations due to the inertia factor in Eq. (43). This ensures that the bound constraints will always be satisfied [17].

The other constraints are handled using the static penalty approach [49]. This procedure prevents infeasible designs from being considered as the optimal solution, while not entirely removing their contribution to the search for the optimal solution.

4. Surrogate based optimization

Structural optimization based on surrogate models substitutes costly structural analyses by cheap to evaluate approximations. These models use a small number of high fidelity response evaluations, by IGA or FEM, to fit an approximate surface to the true function response.

There are three main steps on the building process of a surrogate model [18,20]: selection of the model itself and selection of sampling points, estimation of model parameters, and model testing and validation. These subjects will be discussed in the following.

4.1. Design of experiments

It is important to note that the efficiency and accuracy of the surrogate model depends on the size and quality of the sample used to build the model. In order to be able to provide accurate predictions, the surrogate should be built with as much information as possible. This information can be translated to the sampling points used to fit the surrogate. However, one must balance the number of sampling points, since a greater number of points leads to a more accurate model, but also increases the cost of the model building and evaluation.

In general, the number of points required for the model to provide a sufficiently accurate prediction increases exponentially with the size of the problem. This aspect is known as the *curse of dimensionality*, and is a major concern for sampling techniques. Thereafter, the user may set the initial number of sampling points as a function of the number of variables considered [36,50,51].

If no information about the behavior of the function is given *a priori*, the selection of sampling points is usually done by a Design of Experiments (DoE) technique. This work uses the Latin Hypercube Sampling (LHS) [26–28] to generate the initial sampling of design space. This approach is a stratified random sampling technique where, to generate n sampling points, the design space is equally divided in n rows and n columns, so that each row and each column can only contain one sampling point. Following this rule, the points are then randomly distributed in each interval. This way, the method is able to provide a better uniformity in each dimension when compared with a random distribution [51].

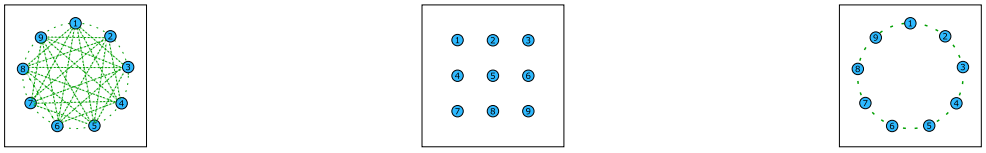

(a) Global (b) Square (c) Ring

Fig. 2. Swarm topologies.

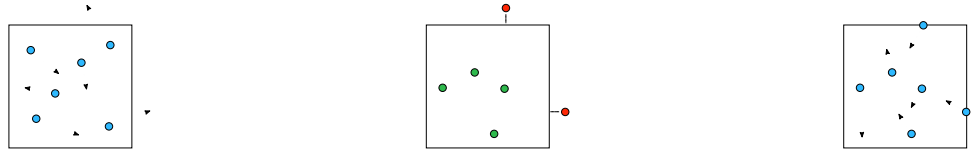

(a) Define the velocity (b) Handle violations (c) New positions

Fig. 3. Boundary constraints handling.

Steponavičė et al. [50] noted that this approach does not guarantee a good uniformity over the whole design space, and large regions may remain unexplored. Optimization techniques can be used to obtain an optimal sampling [18], but the computational cost of this approach may be very high. Therefore, a simple and efficient alternative is adopted in the present work. A LHS algorithm is used to generate a number of samples, and the one that provides the best uniformity is selected to build the initial surrogate. The uniformity be evaluated by a metric such as the *maximin*, where the minimum distance between two sampling points must be maximized [52,18]:

$$d_p\left(\mathbf{x}^{(i)}, \mathbf{x}^{(j)}\right) = \left(\sum_{k=1}^{m} |x_k^{(i)} - x_k^{(j)}|^p\right)^{\frac{1}{p}} \tag{44}$$

where d_p becomes the Euclidean distance when $p = 2$, as usual. This approach will be called LHS$_N$, where N is the number of samples generated. Fig. 4 presents an example of this technique, comparing it to a randomly distributed sample and to a regular LHS. It is noticeable that the LHS$_N$ offers a much more well distributed sample than the other approaches.

4.2. Radial basis functions

Introduced by Hardy [53] for interpolation of topographic data, Radial Basis Functions (RBF) models are widely used in many areas as a simple, but powerful method to approximate multivariate nonlinear functions [36–38].

A RBF model consists of a linear combination of radially symmetric kernel functions ψ centered around a set of sampling points known as the basis function centers. This procedure results in a surface that interpolates the sampling points and whose behavior depends on the basis function chosen in advance.

The basis function response for $\mathbf{x} \in \mathbb{R}^m$ depends basically on the distance between $\mathbf{x}$ and the basis center $\mathbf{c} \in \mathbb{R}^m$, as in:

$$\psi(r) = \psi(||\mathbf{x} - \mathbf{c}||) \tag{45}$$

where the norm $(||\cdot||)$ usually stands for the Euclidian distance. As so, for any function $f(\mathbf{x})$, its RBF prediction $\hat{f}(\mathbf{x})$ can be evaluated by:

$$\hat{f}(\mathbf{x}) = \sum_{j=1}^{n} w_j \psi_j(||\mathbf{x} - \mathbf{c}_j||) \tag{46}$$

where n is the number of centers, $\mathbf{c}_j$ is the jth basis center and w_j is the basis weight. This formulation can also be written as:

$$\hat{f}(\mathbf{x}) = \mathbf{w}^T \boldsymbol{\psi} \tag{47}$$

In this work, all the data will be used in the model building. Therefore, the number of centers is equal to the number of sampling points.

Different basis functions are used in the literature (e.g., linear, cubic, thin plate splines, Gaussian, and multiquadric) [18,20,31]. The most used are the Gaussian basis functions [51], which will be applied in this work as:

$$\psi(r) = \exp\left(-\frac{r^2}{\sigma^2}\right) \tag{48}$$

where $r = ||\mathbf{x} - \mathbf{c}||$ is the radial distance between $\mathbf{x}$ and $\mathbf{c}$ and σ is a parameter known as width, which heavily influences the shape of the function. Since each basis may have a different width, Eq. (48) can be written as:

$$\psi_j(r) = \exp\left(-\frac{||\mathbf{x} - \mathbf{c}_j||^2}{\sigma_j^2}\right) \tag{49}$$

This way, building (or training) a RBF surrogate involves the estimation of the basis widths and the evaluation of the model weights. These steps will be discussed in the following.

4.2.1. Basis width

In the case of the Gaussian function, the width parameter controls the amplitude of its bell-shape, as depicted in Fig. 5.

This behavior means that, for higher width values, the influence exerted by a given sampling point covers a larger region of the design space. Thus, the parameter heavily influences the model prediction. This aspect can be noted in Fig. 6. For small values, the shape resembles a ”needles in a haystack” function, where only regions near sampling points present accurate predictions. In contrast, greater values make the predicted surface smoother than it should be.

Even though the RBF is already a well-established methodology, the estimate of the width of its bases is still a matter of concern for most parametric basis functions, and researchers have not come to an agreement on how it should be done. Thus, many ways to better estimate the parameter have been proposed over the years. The simplest ones derive from the analytical proposal presented in Haykin [54]:

$$\sigma = \frac{d_{max}}{\sqrt{2n}} \tag{50}$$

where d_{max} is the maximum distance between two sampling points. Nakayama et al. [22] tried to generalize this formulation by also considering the number of design variables (m):

$$\sigma = \frac{d_{max}}{\sqrt[m]{mn}} \tag{51}$$

Kitayama et al. [24] propose a slightly different form, where the predicted values are slightly lower for $m > 2$:

$$\sigma = \frac{d_{max}}{\sqrt{m}\sqrt[m]{n}} \tag{52}$$

It should be noted that all of these formulations propose an uniform $\boldsymbol{\sigma}$ vector, where all bases share the same width. However, it is argued that, for non-uniform sampling spaces, a different width should be defined for each basis [24]. Thus, Kitayama et al. [24] also proposes a way to handle these cases:

$$\sigma_j = \frac{d_{j,max}}{\sqrt{m}\sqrt[m]{n-1}} \tag{53}$$

where $d_{j,max}$ is the maximum distance between basis j and the remaining basis considered. Moreover, this work also recommends the use of the Adaptive Scaling technique, where the $\boldsymbol{\sigma}$ vector should be continuously multiplied by a scaling value until $\min(\boldsymbol{\sigma}) \geqslant 1$.

While these techniques are usually able to offer cheap estimations of the width parameter, they do not make any consideration regarding

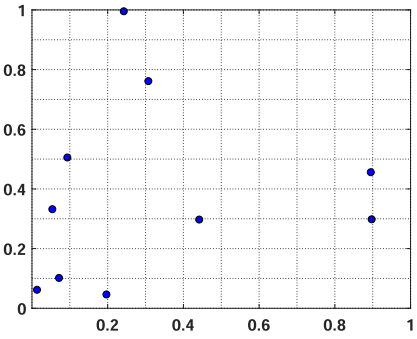

(a) Random distribution

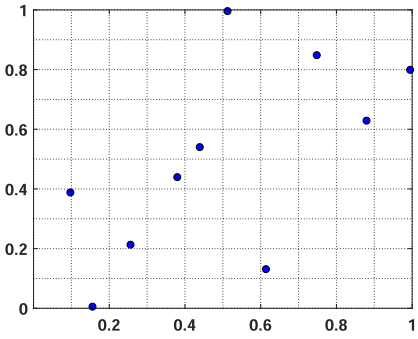

(b) LHS

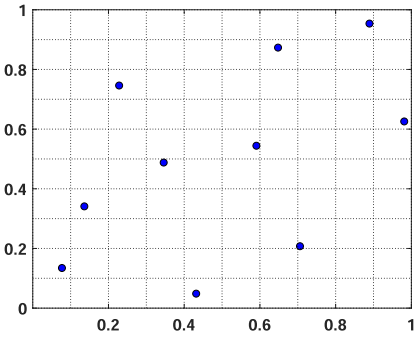

(c) LHS_{20}

Fig. 4. Comparison between DoE techniques.

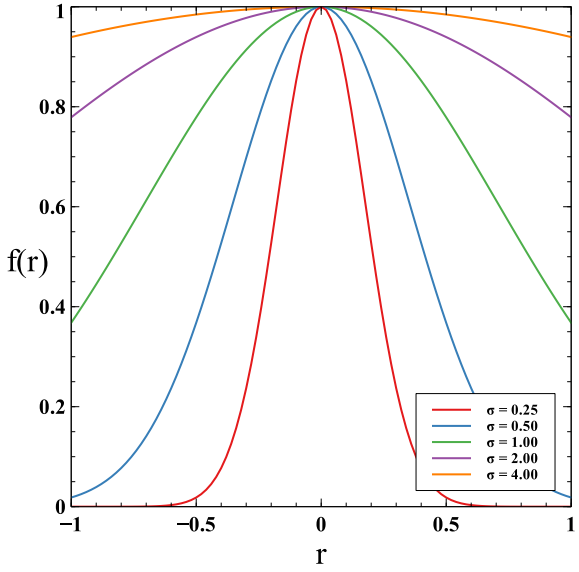

Fig. 5. Gaussian function behavior.

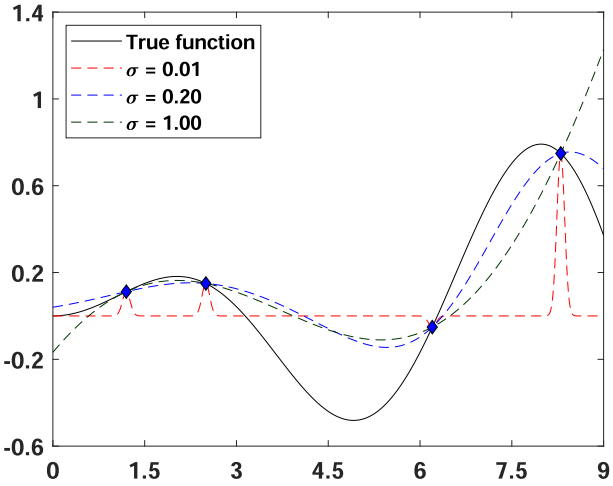

Fig. 6. Model prediction depending on the basis width.

the behavior of the function to be approximated. Therefore, they may be ineffective when compared to other methods.

A more robust approach is to use cross-validation techniques to define the widths. The k-Fold Cross-Validation (k-FCV) is the most common approach, where the sample is divided in k groups, which will be used for training and validation [55]. For each group j, n_w surrogate models are built without the sampling points of that group, where each model corresponds to a trial width. The removed bases are then used as validation points, and the approximation error for each model built is measured by the Root Mean Squared Error:

$$RMSE = \sqrt{\sum_{i=1}^{n_v} \frac{(y_i - \hat{y}_i)^2}{n_v}} \tag{54}$$

where n_v is the number of validation points, y_i is the true response and $\hat{y}_i$ is the predicted response for a given validation point. Finally, the width chosen is the one that provides the lowest sum of MSE. In this paper, an approach based on Sobester et al. [56] is applied, where the trial widths values are in the domain $[10^{-2}, 10] \cdot \sqrt{2}$.

Fig. 7 shows the algorithm to evaluate the σ parameter using k-FCV. At each iteration, $k \cdot n_w$ models have to be built in order to define the

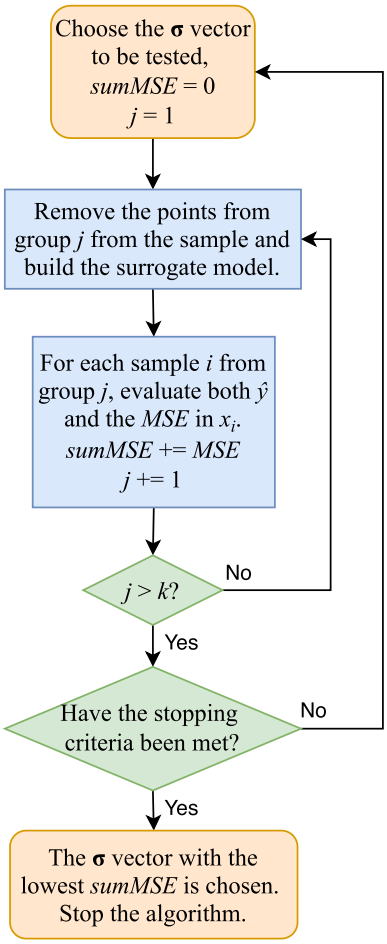

Fig. 7. Cross-validation techniques.

width value, where n_w is the number of trial widths. The most common case of this technique is the Leave-One-Out Cross Validation (LOOCV) [56], where $k = n$. Thus, at each iteration only one sampling point is removed. Although the LOOCV decreases the estimation bias, since the sample being used to fit the model is more similar to the actual sample, the variance also increases [57]. In addition, the computational cost also quickly escalates, especially in larger sampling spaces.

4.2.2. Weights

After defining the $\boldsymbol{\sigma}$ vector, the weights vector $\mathbf{w}$ is evaluated considering that $\hat{y}(\mathbf{x}) = y(\mathbf{x})$ at sampling points. Thus, by interpolation:

$$\begin{bmatrix} \psi_{11} & \psi_{12} & \cdots & \psi_{1n} \\ \psi_{21} & \psi_{22} & \cdots & \psi_{2n} \\ \vdots & \vdots & \ddots & \vdots \\ \psi_{n1} & \psi_{n2} & \cdots & \psi_{nn} \end{bmatrix} \begin{bmatrix} w_1 \\ w_2 \\ \vdots \\ w_n \end{bmatrix} = \begin{bmatrix} y_1 \\ y_2 \\ \vdots \\ y_n \end{bmatrix} \tag{55}$$

This expression can be written in matrix form as:

$$\boldsymbol{\Psi}\mathbf{w} = \mathbf{y} \tag{56}$$

where $\boldsymbol{\Psi}$ is the Gram matrix, whose elements are given by:

$$\psi_{ij} = \exp\left(-\frac{||\mathbf{x}_i - \mathbf{x}_j||^2}{\sigma_j^2}\right) \tag{57}$$

5. Sequential approximate optimization

The Sequential Approximate Optimization (SAO) is an approach proposed by Schmit and Farshi [58] as a way improve the surrogate model along the optimization process. SAO techniques aim to improve the surrogate model including infill points in promising regions of the design space, especially close to the global optimum region.

As the initial sample does not need to accurately represent the true function, it may be relatively small. Thus, this approach reduces the need for a larger initial sample, decreasing the overall computational cost of the optimization [59]. The model will keep on improving until a stopping criteria is met, which can be related to a minimum expected improvement achieved, a minimum error, a given number of stall iterations or a maximum number of high fidelity points evaluated.

The selection of new sampling points often involves both a global search (*exploration*) and a local search (*exploitation*). The former is important to find the global optimum while the latter is important to obtain a fast convergence. This paper will make use of the Expected Improvement, which attempts to balance these two goals [56].

The Expected Improvement (EI) is an error based method which takes advantage of the possible statistical inferences in a Gaussian process. As such, the EI can be applied in any modeling technique based on Gaussian processes. It is often used along with the Kriging model, such as in the well known Efficient Global Optimization (EGO) algorithm [60], but it may also be applied in certain types of SVR and RBF [56,61]. On these, the mean squared error can be estimated by [18]:

$$\hat{s}^2(\mathbf{x}) = \hat{\sigma}^2\left[1 - \boldsymbol{\psi}^T\boldsymbol{\Psi}^{-1}\boldsymbol{\psi} + \frac{1 - \mathbf{1}^T\boldsymbol{\Psi}^{-1}\boldsymbol{\psi}}{\mathbf{1}^T\boldsymbol{\Psi}^{-1}\mathbf{1}}\right] \tag{58}$$

where $\hat{\sigma}^2$ is the the maximum likelihood estimate for the variance:

$$\hat{\sigma}^2 = \frac{(\mathbf{y} - \mathbf{1}\hat{\mu})^T\boldsymbol{\Psi}^{-1}(\mathbf{y} - \mathbf{1}\hat{\mu})}{n} \tag{59}$$

and $\hat{\mu}$ is the maximum likelihood estimate for the mean:

$$\hat{\mu} = \frac{\mathbf{1}^T\boldsymbol{\Psi}^{-1}\mathbf{y}}{\mathbf{1}^T\boldsymbol{\Psi}^{-1}\mathbf{1}} \tag{60}$$

The third term of Eq. (58) is negligible [18] and will be omitted. It is important to note that, if $\mathbf{x}$ is a sampling point, then $\boldsymbol{\psi}$ is a column from $\boldsymbol{\Psi}$ and both $\boldsymbol{\psi}^T\boldsymbol{\Psi}^{-1}\boldsymbol{\psi}$ and $\mathbf{1}^T\boldsymbol{\Psi}^{-1}\boldsymbol{\psi}$ are equal to 1. Therefore, $\hat{s}^2(\mathbf{x}) = 0$.

By considering the uncertainty as a stochastic process, where the variable y has a mean $\hat{y}(\mathbf{x})$ and variance $\hat{s}^2(\mathbf{x})$, the Expected Improvement of a new point $\mathbf{x}$ is given by [18]:

$$\begin{aligned} E[I(\mathbf{x})] = \; & (y_{min} - \hat{y}(\mathbf{x}))\left[\tfrac{1}{2} + \tfrac{1}{2}\operatorname{erf}\left(\tfrac{y_{min} - \hat{y}(\mathbf{x})}{\hat{s}\sqrt{2}}\right)\right] + \\ & \tfrac{\hat{s}}{\sqrt{2\pi}}\exp\left[\tfrac{-(y_{min} - \hat{y}(\mathbf{x}))^2}{2\hat{s}^2}\right] \end{aligned} \tag{61}$$

where y_{min} is the objective function of the best feasible design found so far. An interesting aspect of this formulation is that the first term can related to the exploitation, while the second is related to the exploration [56].

An optimization procedure should be used to find the point $\mathbf{x}$ providing the highest EI, which will then be added to the sample. Since the EI surface can be highly multimodal, the PSO algorithm described in Section 3 will be used to maximize the EI. Fig. 8 depicts the procedure, showing the model improvement with the addition of a new sampling point.

Sobester et al. [56] proposed a slightly modified approach named Weighted Expected Improvement (WEI), where the user is able to control the importance given to either the exploitation or the exploration. This is done by considering a parameter $w \in [0, 1]$:

$$\begin{aligned} WE[I(\mathbf{x})] = \; & w(y_{min} - \hat{y}(\mathbf{x}))\left[\tfrac{1}{2} + \tfrac{1}{2}\operatorname{erf}\left(\tfrac{(y_{min} - \hat{y}(\mathbf{x}))}{\hat{s}\sqrt{2}}\right)\right] + \\ & (1 - w)\tfrac{\hat{s}}{\sqrt{2\pi}}\exp\left[\tfrac{-(y_{min} - \hat{y}(\mathbf{x}))^2}{2\hat{s}^2}\right] \end{aligned} \tag{62}$$

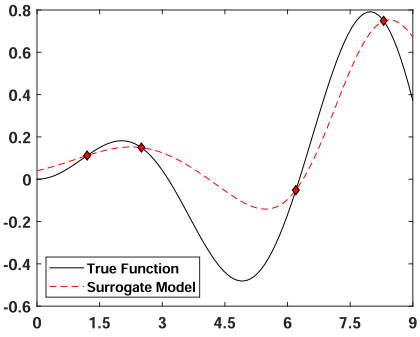

(a) Initial surrogate model

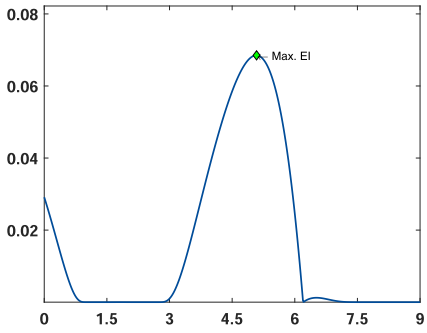

(b) Maximization of the Expected Improvement

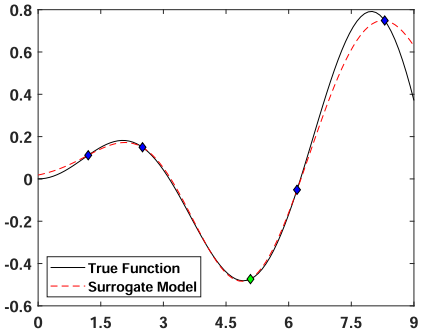

(c) Updated surrogate model

Fig. 8. Addition of the point with the highest EI.

Lower values of w favors the exploration, while larger values favors exploitation. Furthermore, exploration and exploitation retain the same importance when $w \simeq 0.35$ [56]. Hence, the conventional EI, although attempting to balance the two aspects, prioritizes local over global search, which may result in poor results for multimodal functions. In this paper, a cycling approach is employed, where w may assume a value that changes iteratively in the set $[0.1, 0.3, 0.5, 0.7]$, in order to balance exploration and exploitation [56]. The conventional and weighted EI approaches are compared in Section 6.

The EI approaches can be easily adapted for constrained optimization problems where the constraints are exactly evaluated (i.e. without using surrogate models), as in the present work. In this case, the expected improvement of infeasible points is considered equal to 0, which correspond to an exact penalty approach.

6. Numerical examples

This section presents the optimization of different functionally graded plates using the proposed SAO approaches discussed previously. The isogeometric formulation presented in Section 2 is used as the high fidelity model for structural analysis. The mechanical properties of the materials used in the examples are presented in Table 1.

To build the initial surrogate model, only $n = 5$ m sampling points will be generated using the LHS_{20} approach. The surrogate will be improved by the addition of new points until the maximum number of sampling points $n_{max} = 150$ is reached or after 25 iterations of the SAO algorithm without improvement of the solution. Thus, a more computationally expensive approach may be more efficient than the others due to a faster convergence.

Furthermore, a comparative study will be performed by testing out four different width defining methods: the analytical methods proposed by Nakayama et al. [22] and Kitayama et al. [24], and the cross-validation techniques LOOCV and k-FCV, with $k = 5$. These methods will be identified by the acronyms NAK, ASKIT, LOOCV, and 5-FCV, respectively. In addition, results will be shown for both the EI and the WEI to study the effect of these two different SAO approaches on the optimization process.

For each optimization problem, $N_r = 10$ runs will be carried out and the different approaches will be characterized by three different metrics. The first one is the average number of points evaluated until the algorithm is stopped (n_p), indicating how quickly the algorithm finds the optimum solution. The second one is the average Normalized Root Mean Squared Error:

$$\overline{NRMSE} = \frac{1}{N_r} \sum_{i=1}^{N_r} \sqrt{\frac{(y_{min} - \hat{y}_i)^2}{y_{min}^2}} \tag{63}$$

where y_{min} is the objective function of the optimum design and $\hat{y}_i$ is the best objective function found by the algorithm in the i-th run. This metric evaluates the accuracy of the approach. Finally, the algorithm efficiency is evaluated using the Speed-up:

$$\text{Speed} - \text{up} = \frac{1}{N_r} \sum_{i=1}^{N_r} \frac{T_{HFM}}{T_{SUR,\,i}} \tag{64}$$

where T_{HFM} is the time spent on the conventional optimization and $T_{SUR,\,i}$ is the time spent on each proposed SAO approach, on the i-th run, both measured by the wall-clock time. This contemplates the

Table 1
Material properties.

Material	E (GPa)	ν	ρ (kg/m^3)
Al	70.00	0.3	2707
SUS304	201.04	0.3	8166
Al_2O_3	380.00	0.3	3800
Si_3N_4	348.43	0.3	2370

whole process, considering the time spent on high fidelity evaluations, surrogate model building and the optimization process itself.

The Ring topology is considered in the PSO due to its reliability. Unless stated in a particular example, the optimization parameters are $Stall_{max} = 25, N_p = 50, w = 0.7, \quad c_1 = 1.5, c_2 = 1.5,$ and $p_{mut} = 0.05$. Since surrogates are cheap to evaluate and EI surface can be highly multimodal, $It_{max} = 500$ is used to find the new sampling points by EI maximization. All numerical computations were performed on a computer core i7-5500U CPU of 2.4 GHz clock speed and 16 GB of RAM. No parallelization procedure was used.

6.1. Analysis validation

This section presents the validation of the presented IGA formulation using two numerical examples. The first example corresponds to the computation of the critical load of a clamped square plate with $a/h = 100$, where a is the plate length. The boundary conditions were used as specified in Auad et al. [46] and a 8×8 cubic NURBS mesh is used for structural analysis. The material properties are $E_m = 207.79$ GPa, $\nu_m = 0.28, E_c = 322.27$ GPa, and $\nu_c = 0.28$. The effective properties are estimated via the RoM and the volume fraction is described by the Power-law function:

$$V_c(z) = \left(\frac{1}{2} + \frac{z}{h}\right)^p \tag{65}$$

where the p exponent controls the material gradation. The non-dimensional buckling load ($\lambda_{norm} = N_{cr}a^2/(\pi^2 D_c)$, where $D_c = E_c h^3/\left[12(1-\nu_c^2)\right]$) is compared with the results found by Bateni et al. [62]. The obtained results shown in Table 2 are in excellent agreement of the reference results.

The second example deals with the fundamental frequency of a simple supported square plate with $a/h = 10$ and made of SUS304/Si_3N_4. A 8×8 cubic NURBS mesh is adopted for structural analysis. The effective properties are estimated via the Mori-Tanaka scheme and the volume fraction variation is described by the Power-law function for different values of the p index. The non-dimensional natural frequency ($\omega_{norm} = \omega h\sqrt{\rho_c/G_c}$, where $G_c = E_c/[2(1+\nu_c)]$) is compared with the results found by Nguyen et al. [63], as shown in Table 3. Once again, an excellent agreement is found with respect to the reference results.

6.2. Example 1

This example deals with maximization of the buckling load of a simply supported square plate made of Al as metal and Al_2O_3 as ceramic (Al/Al_2O_3), with $a/h = 10$, subjected to a uniform compressive load N_x. Fig. 9 shows the loading and boundary conditions of the functionally graded plate. A 16×16 cubic NURBS mesh is used in the isogeometric analysis.

The properties are estimated via the Mori-Tanaka model. The gradation is defined by 9 control points through the thickness, symmetric with respect to the mid-plane. Thus, this problem has 5 design variables. A constraint is considered to limit the a maximum percentage of ceramic material:

Table 2
Non-dimensional buckling load of a clamped FG square plate.

p	Bateni et al. [62]	Present	Difference
0	10.0571	10.0686	0.11%
0.5	8.6538	8.6817	0.32%
1	8.1424	8.1798	0.46%
2	7.7745	7.8136	0.50%
3	7.6173	7.6514	0.45%
5	7.4275	7.4527	0.34%

Table 3
Non-dimensional fundamental frequency of a simply supported FG square plate.

p	Nguyen et al. [63]	Present	Difference
1	0.0542	0.0545	0.55%
2	0.0485	0.0487	0.41%
5	0.0438	0.0439	0.23%
10	0.0416	0.0416	0.00%

$$g_1(\mathbf{x}) = \overline{V}_c(\mathbf{x}) - \overline{V}_{c,max} \leqslant 0 \tag{66}$$

where:

$$\overline{V}_c(\mathbf{x}) = \frac{1}{h}\int_{-h/2}^{h/2} V_c \, dz \tag{67}$$

This integral is evaluated using Gaussian quadrature with 10 points.

The optimization problem is given by

$$\begin{cases} \text{maximize} & N_{cr}(\mathbf{x}) \\ \text{subjected to} & g_1(\mathbf{x}) \leqslant 0 \\ \text{with} & \mathbf{0} \leqslant \mathbf{x} \leqslant \mathbf{1} \end{cases} \tag{68}$$

where N_{cr} is the critical buckling load. The problem was proposed by Do et al. [15], where a Deep Neural Network (DNN) was used as a surrogate model to improve the efficiency of the process. Ten thousand sampling points were evaluated, with 80% for training and 20% for validation. The authors considered three different cases, with $\overline{V}_{c,max}$ equal to 35%, 50% and 65%.

In the present work, the optimization was carried out using the PSO algorithm with $It_{max} = 75$. Table 4 presents the optimal designs found using the conventional approach (PSO + IGA) and the best SAO approach for each case. These results are compared to the best design found by the DNN [15]. The non-dimensional buckling load is given by $\lambda_{norm} = N_{cr}a/D_m$, where $D_m = E_m h^3/\left[12(1-\nu_m^2)\right]$. It can be noted that the the optimal designs are very similar, but the reference λ_{norm} is slightly lower than the results obtained in this work. This small difference may be explained by the use of a Third-order Shear Deformation Theory (TSDT) by the reference.

In this example, all width-defining methods, coupled with the EI and the WEI, achieved the optimal design. The best SAO approaches were defined by their success rate and Speed-up, and these were the WEI with the ASKIT for $\overline{V}_{c,max} = 35\%$, the WEI with the 5-FCV for $\overline{V}_{c,max} = 50\%$, and the EI with the 5-FCV for $\overline{V}_{c,max} = 65\%$. The average SAO perfomance, shown in Table 4 in terms of the average time spent, number of iterations ($\overline{N}_{iter}$) and number of evaluations ($\overline{n}_p$), refers to these combinations. Therefore, the SAO approaches present in this work can dramatically reduce the computational cost (up to 97%) with respect to the conventional approach based on the use of high fidelity computational methods for structural analysis, without compromising the solution accuracy.

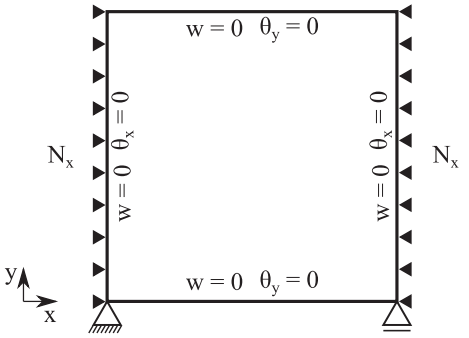

Fig. 9. Simply support FGM plate.

Table 4
Optimal designs for Example 1.

Design variable	$\overline{V}_{c,max}$ = 35%			$\overline{V}_{c,max}$ = 50%			$\overline{V}_{c,max}$ = 65%		
	HFM	DNN [15]	SAO	HFM	DNN [15]	SAO	HFM	DNN [15]	SAO
1	1.0	1.0	1.0	1.0	1.0	1.0	1.0	1.0	1.0
2	1.0	1.0	1.0	1.0	1.0	1.0	1.0	1.0	1.0
3	0.4000	0.4003	0.4000	1.0	0.9880	0.9999	1.0	1.0	1.0
4	0.0	0.0	0.0	0.0	0.0	0.0	0.4500	0.4420	0.4500
5	0.0	0.0	0.0	0.0	0.0	0.0	0.0	0.0	0.0
λ_{norm}	11.634	11.185	11.634	15.357	14.603	15.357	16.705	16.193	16.705
Difference		0.490%	0.002%		0.748%	0.003%		1.029%	0.001%
$\overline{N}_{iter}$	75		28	71		28	65		28
$\overline{n}_p$	3750		53	3550		53	3250		53
Average time	1088 s		26 s	1024 s		26 s	939 s		27 s

The metrics obtained for the proposed SAO approaches are shown in Table 5. Fig. 10 presents boxplots comparing all results found for all methodologies. The red × inside each boxplot refers to the average value.

The results obtained using the SAO approaches were excellent. Overall, the error found was much lower than the one found on Do et al. [15], which needed ten thousand sampling points to build and test the neural network beforehand. This shows the efficiency of the SAO technique, which is able to obtain designs very close to the optimum after few iterations. In fact, most approaches achieved the global optimum after less than 55 high fidelity evaluations, including the initial sample. Moreover, the robustness of the SAO approaches is noticeable by taking a closer look at Fig. 10, especially for ASKIT, LOOCV, and 5-FCV. These methods showed a very small dispersion from the optimal result, except for a few outliers.

Although the cross-validation methods provided better approximations, the analytical formulations also achieved the global optimum in most cases. All algorithms significantly decreased the optimization time with respect to the conventional optimization. However, ASKIT and 5-FCV were more efficient than NAK and LOOCV. The most accurate approaches were ASKIT, LOOCV, and 5-FCV. Finally, the performance of conventional (EI) and weighted expected improvement (WEI) was similar.

6.2.1. Enforcing a smooth optimum design

An interesting aspect of the results presented previously is that B-Splines provide a continuous material gradation, but this gradation may not be smooth enough to avoid stress concentrations. Thus, to ensure a design that keeps the advantages of FGMs over laminated structures, it might be necessary to add constraints to enforce a smooth gradation.

Therefore, this work includes a constraint limiting the rate of change of the volume fraction through the plate thickness:

$$g_2(\mathbf{x}) = \left|\frac{dV_c}{dr}\right| - \tan(\theta_{max}) \leqslant 0 \tag{69}$$

where $r = z/h$ and θ_{max} was chosen as 75°. Smoother gradations can be obtained using smaller θ_{max}.

Optimization is carried out using PSO with It_{max} = 150. The optimal gradations through the thickness, in the three cases, are shown in Fig. 11, as well as the results found previously without considering g_2.

Table 5
Metrics for Example 1 using the proposed SAO approaches.

$\overline{V}_{c,max}$	SAO approach	Width	$\overline{n}_p$	$\overline{NRMSE}$	Speed-up
35%	EI	NAK	77	0.04%	17.89
		ASKIT	**52**	**0.00**%	40.75
		LOOCV	**52**	**0.00**%	24.45
		5-FCV	53	**0.00**%	**42.67**
	WEI	NAK	85	0.11%	16.97
		ASKIT	53	**0.00**%	**41.37**
		LOOCV	55	0.03%	15.54
		5-FCV	**52**	**0.00**%	39.14
50%	EI	NAK	79	**0.00**%	15.24
		ASKIT	53	**0.00**%	**34.84**
		LOOCV	**52**	**0.00**%	22.91
		5-FCV	54	**0.00**%	32.93
	WEI	NAK	80	0.03%	17.48
		ASKIT	53	**0.00**%	37.24
		LOOCV	**52**	**0.00**%	23.33
		5-FCV	53	0.44%	**39.24**
65%	EI	NAK	80	0.23%	14.41
		ASKIT	**53**	**0.00**%	33.79
		LOOCV	55	**0.00**%	14.19
		5-FCV	**53**	**0.00**%	**34.92**
	WEI	NAK	89	0.09%	12.90
		ASKIT	**54**	1.00%	**32.85**
		LOOCV	**54**	**0.00**%	15.60
		5-FCV	55	**0.00**%	31.74

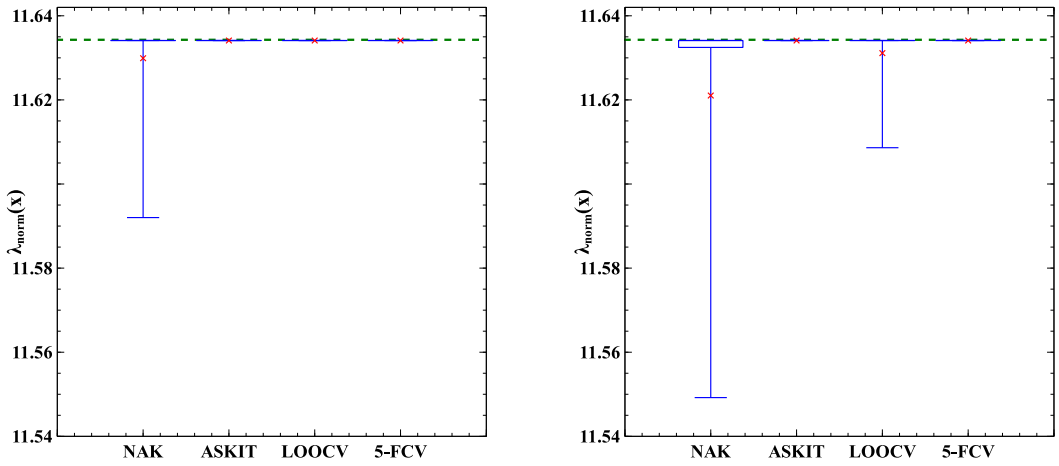

(a) EI, $\overline{V}_{c,max} = 35\%$

(b) WEI, $\overline{V}_{c,max} = 35\%$

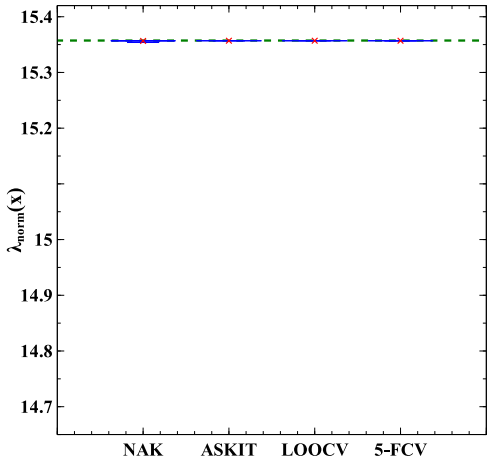

(c) EI, $\overline{V}_{c,max} = 50\%$

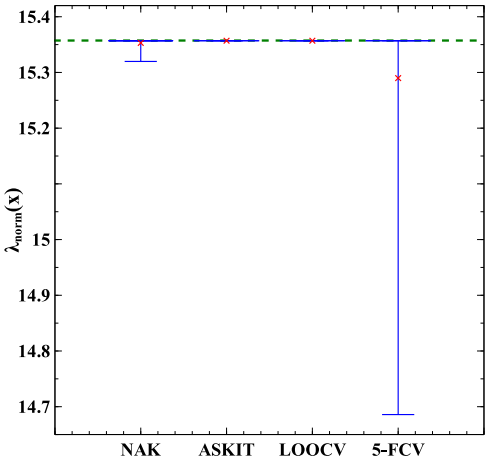

(d) WEI, $\overline{V}_{c,max} = 50\%$

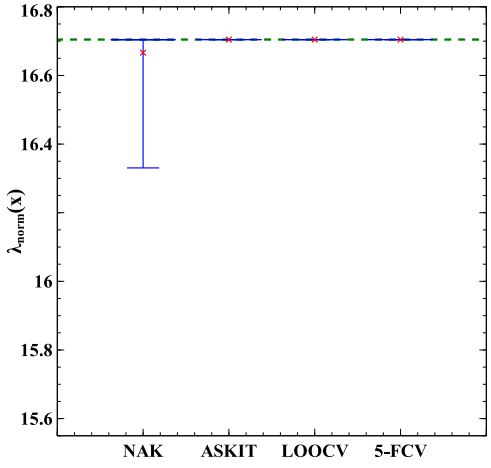

(e) EI, $\overline{V}_{c,max} = 65\%$

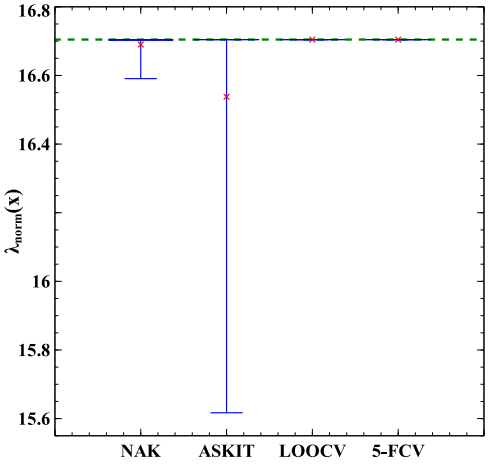

(f) WEI, $\overline{V}_{c,max} = 65\%$

Fig. 10. Results of proposed SAO approaches for Example 1.

The difference in the optimal design is more noticeable for $\overline{V}_{c,max} = 50\%$, where it is clear that the new design is much smoother. In the other cases, the difference is small. When $\overline{V}_{c,max} = 65\%$, the optimal design did not change, as the new constraint is inactive. It is interesting to note that the decrease in the objective function, when compared to the optimization without this constraint, was relatively small (3.31% for $\overline{V}_{c,max} = 35\%$ and 5.57% for $\overline{V}_{c,max} = 50\%$).

The optimal designs are shown in Table 6. All SAO approaches managed to find designs very close to the optimal solution. The overall best approaches, defined by their success rate and the speed-up, were

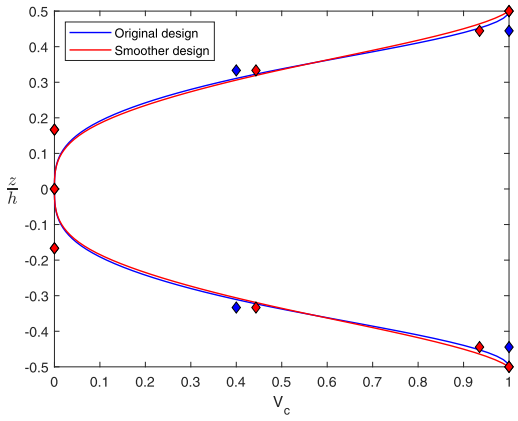

(a) $\overline{V}_{c,max} = 35\%$

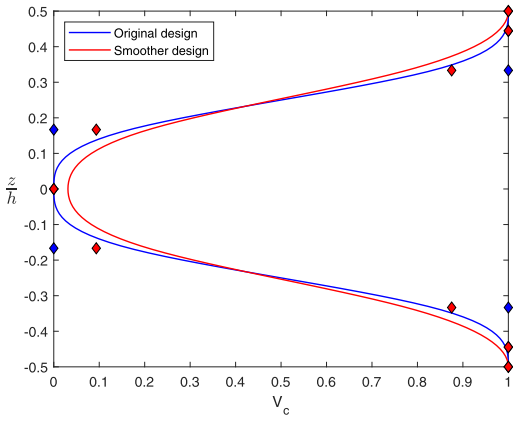

(b) $\overline{V}_{c,max} = 50\%$

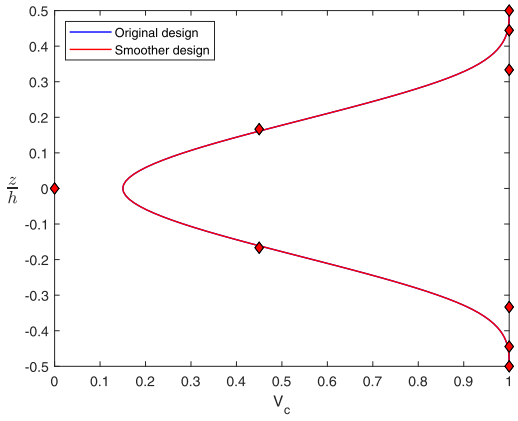

(c) $\overline{V}_{c,max} = 65\%$

Fig. 11. Optimal gradation for Example 1 with smooth design constraint.

Table 6
Optimal designs for Example 1 with smooth design constraint.

Design variables	$\overline{V}_{c,max} = 35\%$		$\overline{V}_{c,max} = 50\%$		$\overline{V}_{c,max} = 65\%$	
	HFM	SAO	HFM	SAO	HFM	SAO
1	1.0	1.0	1.0	1.0	1.0	1.0
2	0.9351	0.9352	1.0	1.0	1.0	1.0
3	0.4433	0.4432	0.8753	0.8754	1.0	1.0
4	0.0	0.0	0.0935	0.0934	0.4500	0.4500
5	0.0	0.0	0.0	0.0	0.0	0.0
λ_{norm}	11.249	11.251	14.564	14.564	16.705	16.704
Difference		0.011%		0.003%		0.001%
$\overline{N}_{iter}$	116	27	118	28	74	27
$\overline{n}_p$	5800	52	5900	53	3700	52
Average time	1477 s	63 s	1572 s	54 s	935 s	52 s

EI with ASKIT for $\overline{V}_{c,max} = 35\%$, WEI with ASKIT for $\overline{V}_{c,max} = 50\%$ and WEI with 5-FCV for $\overline{V}_{c,max} = 65\%$.

The metrics obtained for the proposed approaches are shown in Table 7. The results show that the consideration of the new constraint makes the optimization problem more difficult to solve, but the SAO procedures still quickly found the optimum design, keeping a high computational efficiency. Most cases achieved the global optimum after less than 60 high fidelity evaluations. Another interesting aspect is that all tested SAO approaches managed to find a slightly better optimal design than the conventional algorithm for $\overline{V}_{c,max} = 35\%$, which shows the accuracy and efficiency of the SAO approaches. The relative performance of SAO approaches was similar to the case without the smooth design constraint. However, the consideration of this constraint reduces the speed-up of SAO approaches.

6.3. Example 2

The example consists in the maximization of the fundamental frequency of a simply supported square plate with $a/h = 10$. The geometry and boundary conditions are the same shown is Figure 9, but the plate is made of SUS304/Si_3N_4. Homogenization is carried out by the Mori-Tanaka model and a 16×16 cubic NURBS mesh is used in the isogemetric analysis.

Table 7
Metrics for Example 1 with smooth design constraint.

$\overline{V}_{c,max}$	SAO approach	Width	$\overline{n}_p$	$\overline{NRMSE}$	Speed-up
35%	EI	NAK	84	0.16%	10.07
		ASKIT	**52**	**0.01**%	**23.45**
		LOOCV	53	**0.01**%	19.65
		5-FCV	54	0.28%	22.94
	WEI	NAK	82	0.50%	10.51
		ASKIT	**53**	**0.01**%	23.23
		LOOCV	56	0.46%	18.94
		5-FCV	**53**	1.71%	**29.43**
50%	EI	NAK	76	0.82%	12.08
		ASKIT	**53**	0.52%	24.91
		LOOCV	57	**0.05**%	16.79
		5-FCV	54	0.41%	**24.95**
	WEI	NAK	83	0.58%	11.25
		ASKIT	**53**	**0.00**%	**29.32**
		LOOCV	55	**0.00**%	18.45
		5-FCV	57	0.01%	23.32
65%	EI	NAK	74	0.12%	6.91
		ASKIT	53	**0.00**%	14.74
		LOOCV	**52**	**0.00**%	11.89
		5-FCV	**52**	0.12%	**17.70**
	WEI	NAK	80	0.50%	6.93
		ASKIT	54	**0.00**%	15.03
		LOOCV	56	0.15%	9.90
		5-FCV	**52**	**0.00**%	**17.98**

Table 8
Optimal designs for Example 2.

Design variables	$\overline{V}_{c,max}$ = 35%			$\overline{V}_{c,max}$ = 50%			$\overline{V}_{c,max}$ = 65%		
	HFM	DNN [15]	SAO	HFM	DNN [15]	SAO	HFM	DNN [15]	SAO
1	1.0	1.0	1.0	1.0	1.0	1.0	1.0	1.0	1.0
2	1.0	1.0	1.0	1.0	1.0	1.0	1.0	1.0	1.0
3	1.0	1.0	1.0	1.0	1.0	1.0	1.0	1.0	1.0
4	0.2501	0.2480	0.2500	0.9999	1.0	0.9998	1.0	1.0	1.0
5	0.0	0.0	0.0	0.0	0.0070	0.0	0.7497	0.7530	0.7497
6	0.0	0.0	0.0	0.0	0.0	0.0	0.0	0.0	0.0
7	0.0	0.0	0.0	0.0	0.0	0.0	0.0	0.0	0.0
ω_{norm}	0.0534	0.0531	0.0534	0.0601	0.0600	0.0601	0.0671	0.0669	0.0671
Difference		0.188%	0.003%		0.170%	0.011%		0.149%	0.001%
$\overline{N}_{iter}$	88		55	83		49	93		52
$\overline{n}_p$	4400		90	4150		84	4650		87
Average time	1303 s		50 s	1238 s		71 s	2157 s		78 s

Here, the volume fraction gradation is defined by 13 control points, symmetric about the mid-plane, resulting in 7 design variables. A maximum volume fraction of ceramic material is considered, as in Equation (66), where $\overline{V}_{c,max}$ may be either 35%, 50% or 65%. The problem may be stated as:

$$\begin{cases} \text{maximize} & \omega(\mathbf{x}) \\ \text{subjected to} & g_1(\mathbf{x}) \leqslant 0 \\ \text{with} & \mathbf{0} \leqslant \mathbf{x} \leqslant \mathbf{1} \end{cases} \tag{70}$$

The optimization was carried out using PSO with $It_{max} = 100$ and the proposed SAO approaches. The obtained optimal designs are shown in Table 8, where they are compared to the best design found by using DNN as surrogate model [15]. The non-dimensional natural frequency is given by $\omega_{norm} = \omega h\sqrt{\rho_c/G_c}$, where $G_c = E_c/[2(1+\nu_c)]$. The most accurate SAO approaches, which achieved the best design for each case, were EI with ASKIT for $\overline{V}_{c,max}$ = 35%, WEI with ASKIT for $\overline{V}_{c,max}$ = 50%, and WEI with ASKIT for $\overline{V}_{c,max}$ = 65%. The average SAO perfomance shown in Table 8 corresponds to these approaches.

The metrics obtained for the proposed SAO approaches are shown in Table 9, while the graphic representation using boxplots is presented in Fig. 12.

Once again, most SAO results were excellent. The use of NAK approach for width-definition was the exception, as it struggled to find the global optimum. Nevertheless, most methods did find results more accurate than the ones presented, in Do et al. [15], although the deviation from the optimal design was often greater than in the first example.

It is interesting to note that, due to quickly selecting new sampling points close to the global optimum, the 5-FCV approach presented the fastest convergence, showing a good accuracy while also having a speed-up greater than 20 when associated with both EI and WEI approaches. The LOOCV yielded similar results, albeit at a much higher computational cost. In terms of accuracy, the best overall method was ASKIT, which achieved the lowest errors in all cases except for $\overline{V}_{c,max}$ = 65%, when it was outperformed by the LOOCV. This trend can also be analyzed on Fig. 12. The ASKIT was more robust for the cases where $\overline{V}_{c,max}$ = 35% and $\overline{V}_{c,max}$ = 50%, where it presented the lowest dispersion from the optimal design, while LOOCV presented results slightly closer to the optimum in the last case. However, due to its slower convergence, ASKIT was also surpassed by the 5-FCV in terms of efficiency. Once more, both EI and WEI approaches showed similar results.

Table 9
Metrics for Example 2 using the proposed SAO approaches.

$\overline{V}_{c,max}$	SAO approach	Width	$\overline{n}_p$	$\overline{NRMSE}$	Speed-up
35%	EI	NAK	102	4.90%	12.02
		ASKIT	90	**0.13**%	15.95
		LOOCV	**66**	0.23%	13.42
		5-FCV	72	0.53%	**23.10**
	WEI	NAK	92	4.70%	14.89
		ASKIT	81	**0.04**%	19.83
		LOOCV	69	0.35%	9.48
		5-FCV	**68**	0.59%	**25.96**
50%	EI	NAK	107	5.36%	10.72
		ASKIT	83	**0.01**%	17.55
		LOOCV	**64**	0.02%	14.61
		5-FCV	70	0.12%	**22.83**
	WEI	NAK	71	6.42%	**23.44**
		ASKIT	84	**0.01**%	17.38
		LOOCV	**64**	0.04%	16.22
		5-FCV	70	0.14%	22.46
65%	EI	NAK	102	4.94%	12.00
		ASKIT	90	0.27%	16.09
		LOOCV	**66**	**0.16**%	19.23
		5-FCV	74	0.42%	**22.36**
	WEI	NAK	84	4.62%	18.70
		ASKIT	87	0.24%	17.49
		LOOCV	89	**0.18**%	16.78
		5-FCV	**71**	0.32%	**25.72**

6.3.1. Enforcing a smooth optimum design

In order to ensure a more smooth volume fraction variation, the optimization is carried out considering the constraint given by Eq. (69) with $\theta_{max} = 75^{\circ}$. The optimization problem is given by:

$$\begin{cases} \text{maximize} & \omega(\mathbf{x}) \\ \text{subjected to} & g_1(\mathbf{x}) \leqslant 0 \\ & g_2(\mathbf{x}) \leqslant 0 \\ \text{with} & \mathbf{0} \leqslant \mathbf{x} \leqslant \mathbf{1} \end{cases} \tag{71}$$

The optimization was performed using PSO algorithm with $It_{max} = 200$ considering both the high fidelity and the proposed SAO approaches. The obtained optimal designs are shown in Table 10, while the optimum material gradation is depicted in Fig. 13. The optimum design without considering g_2 shows a sharp transition from the ceramic rich to the metal rich parts with the increase of the number of control points. The optimal solution tends to a sandwich plate, especially for small $\overline{V}_{c,max}$ values. By considering the additional constraint, the optimum designs are much smoother. Furthermore, the decrease in the ω_{norm} is negligible: only 0.925% for $\overline{V}_{c,max} = 35\%$, 1.056% for $\overline{V}_{c,max} = 50\%$, and 0.527% for $\overline{V}_{c,max} = 65\%$. Hence, the consideration of a smoother design implies only a small reduction in the fundamental frequency.

The best approaches, in terms of accuracy, were EI with ASKIT for $\overline{V}_{c,max} = 35\%$, WEI with ASKIT for $\overline{V}_{c,max} = 50\%$, and EI with ASKIT for $\overline{V}_{c,max} = 65\%$. The SAO average performance shown in Table 10 refers to these cases. Once again, the SAO approaches achieved a decrease of more than 90% in the computational time compared to the conventional approach based on the use of high fidelity computational methods for structural analysis, without compromising the solution accuracy.

Finally, the metrics obtained for the proposed approaches are presented in Table 11. This time, the increased problem complexity did affect the SAO approaches, as the $\overline{NRMSE}$ is noticeably higher in some cases. However, most results were still very good. Once again, 5-FCV achieved the highest Speed-up due to its faster convergence, while ASKIT approach achieved the lowest errors. Furthermore, most approaches achieved convergence after less than 90 high fidelity evaluations. Finally, the results obtained by both EI and WEI were also similar.

6.4. Example 3

This example deals with the maximization of the buckling load of a clamped square plate with $a = 0.72$ m and a hole of radius $r = a/10$ in its center. The plate is made of SUS304/Si_3N_4 and the effective mechanical properties are once again estimated via the Mori-Tanaka scheme. The isogeometric analysis is conducted with a cubic NURBS mesh with 512 elements. Fig. 14 depicts the loading, boundary conditions, and isogemetric mesh.

The material gradation is defined by 9 control points, symmetric at the mid-plane. The plate thickness is also taken as a design variable in this example. Hence, there are six design variables. In addition to the ceramic volume fraction constraint, as in Equation (66), a mass constraint will also be considered as:

$$g_2(\mathbf{x}) = \left(a^2 - \pi r^2\right) \int_{-h/2}^{h/2} \rho(z)\ dz - m_{max} \leqslant 0 \tag{72}$$

where $\rho(z)$ is the effective density at the coordinate z estimated using the Voigt model and m_{max} is the maximum mass allowed. In this case, $m_{max} = 100$ kg. Considering these aspects, the optimization problem is defined as:

$$\begin{cases} \text{maximize} & N_{cr}(\mathbf{x}) \\ \text{subjected to} & g_1(\mathbf{x}) \leqslant 0 \\ & g_2(\mathbf{x}) \leqslant 0 \\ \text{with} & h_{min} \leqslant x_1 \leqslant h_{max} \\ & 0 \leqslant x_i \leqslant 1 \quad \text{for } i = 2, 3, \ldots 6 \end{cases} \tag{73}$$

where $h_{min} = 0.01$ m and $h_{max} = 0.05$ m.

Table 12 presents the optimal design achieved using the different approaches for each case, where $V_{c,i}$ is the value found for the i-th control point. In terms of accuracy, the best performing SAO techniques were the WEI with ASKIT for $\overline{V}_{c,max} = 35\%$, the EI with ASKIT for $\overline{V}_{c,max} = 50\%$ and the WEI with ASKIT for $\overline{V}_{c,max} = 65\%$. The results shown in the table correspond to these methods, and Figure 15 shows their convergence history. In terms of number of iterations, it is clear that the SAO does converge much sooner than the conventional algorithm. It is important to remember that a SAO iteration evaluates the

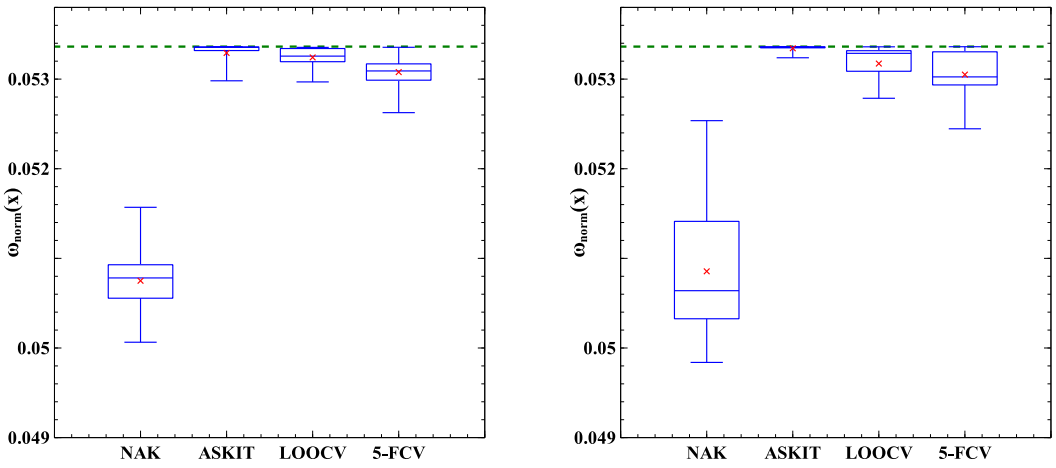

(a) EI, $\overline{V}_{c,max} = 35\%$

(b) WEI, $\overline{V}_{c,max} = 35\%$

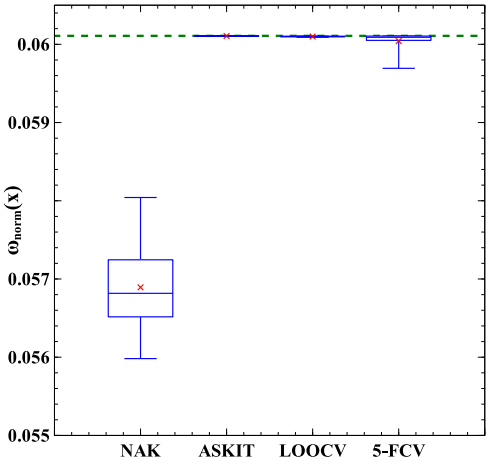

(c) EI, $\overline{V}_{c,max} = 50\%$

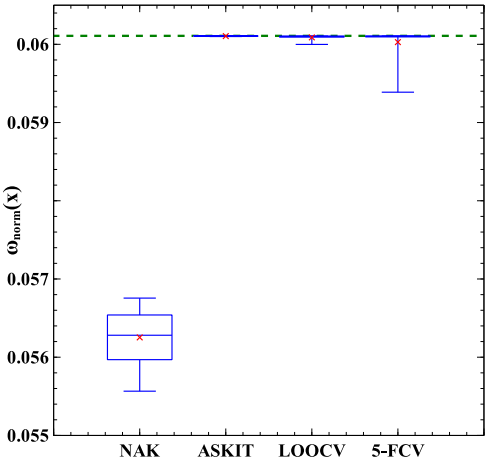

(d) WEI, $\overline{V}_{c,max} = 50\%$

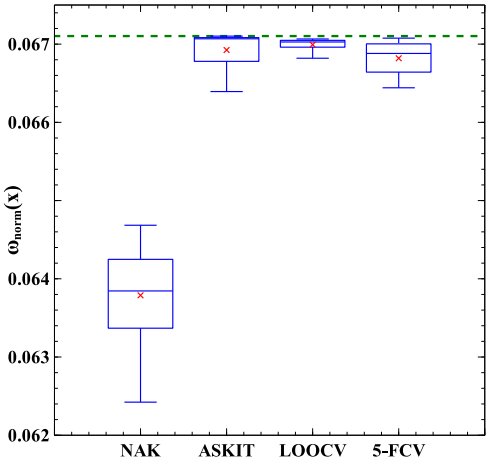

(e) EI, $\overline{V}_{c,max} = 65\%$

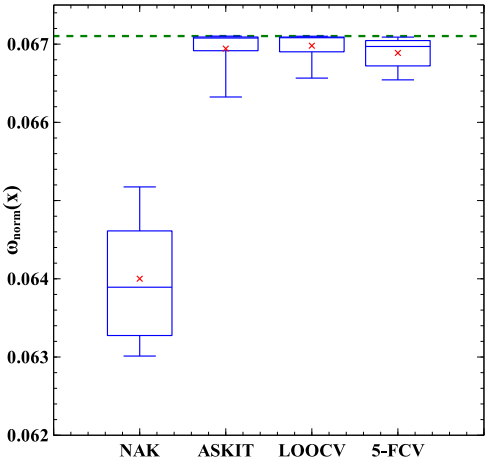

(f) WEI, $\overline{V}_{c,max} = 65\%$

Fig. 12. Results on all approaches tested for Example 2.

high fidelity model using IGA only once, while the conventional PSO does it $N_p = 50$ times. These aspects imply that the time spent using SAO is lower than using the PSO by orders of magnitude, which can be seen in Table 12. It is interesting to note that all constraints remain active, in all cases. Once again, the SAO approach was capable of finding even better designs than the conventional optimization.

Table 13 shows the metrics related to the SAO approaches for this example and Fig. 16 presents the boxplot representation for each of

Table 10
Optimal designs for Example 2 with smooth design constraint.

Design variables	$\overline{V}_{c,max}$ = 35%		$\overline{V}_{c,max}$ = 50%		$\overline{V}_{c,max}$ = 65%	
	HFM	SAO	HFM	SAO	HFM	SAO
1	1.0	0.9980	1.0	0.9981	1.0	0.9985
2	0.9995	0.9962	1.0	0.9968	0.9997	0.9979
3	0.7601	0.7455	1.0	0.9962	0.9989	0.9993
4	0.4107	0.4098	0.6980	0.6933	0.9563	0.9565
5	0.0189	0.0315	0.3019	0.3073	0.5809	0.5413
6	0.0005	0.0006	0.0	0.0034	0.2138	0.2501
7	0.0	0.0018	0.0	0.0013	0.0	0.0
ω_{norm}	0.0529	0.0528	0.0595	0.0594	0.0667	0.0667
Difference		0.123%		0.073%		0.137%
$\overline{N}_{iter}$	180	55	150	46	150	52
$\overline{n}_p$	9000	90	7500	81	7500	87
Average time	2419 s	205 s	2168 s	166 s	2157 s	191 s

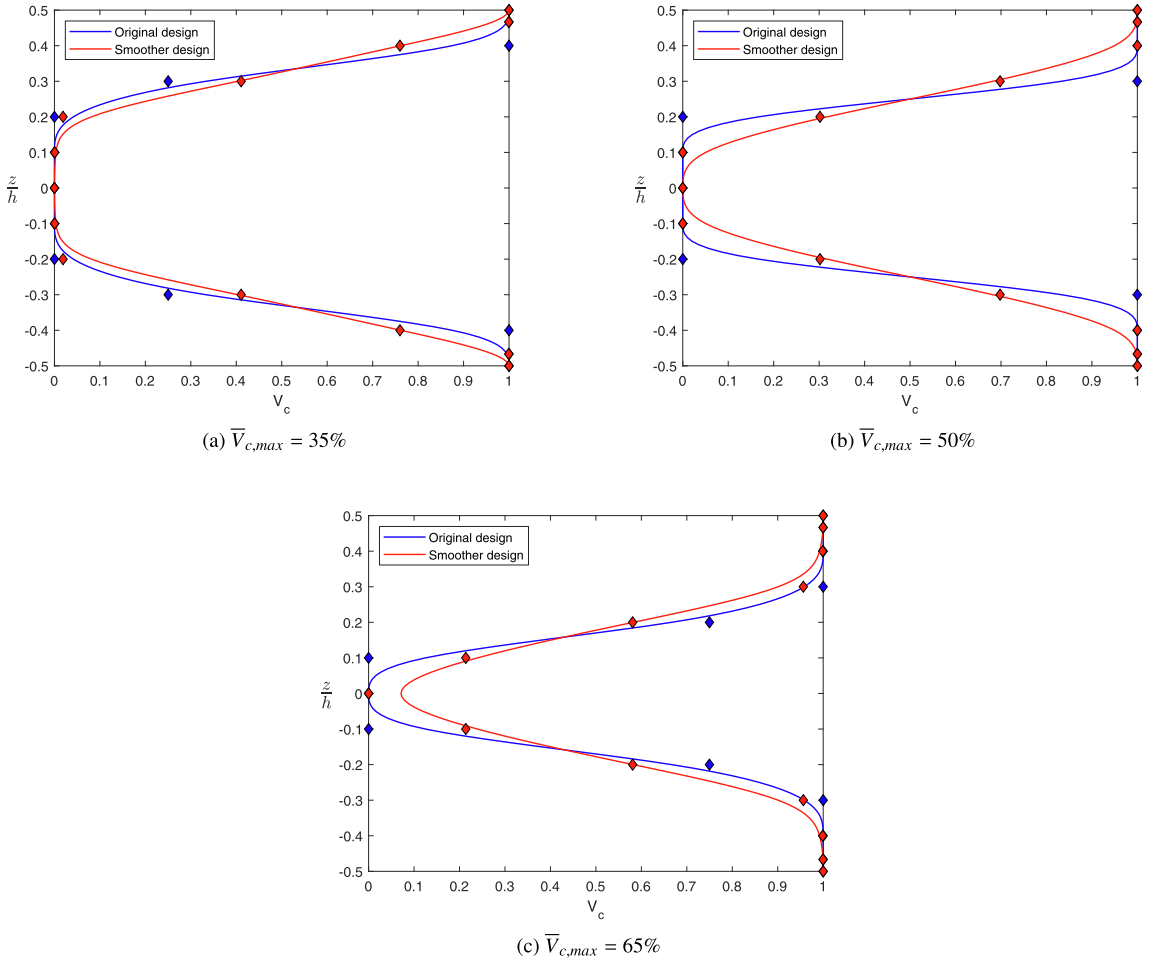

(a) $\overline{V}_{c,max}$ = 35%

(b) $\overline{V}_{c,max}$ = 50%

(c) $\overline{V}_{c,max}$ = 65%

Fig. 13. Optimal gradation for Example 1 with smooth design constraint.

them. In this example, the consideration of a more complex structure results in the increase of the structural analysis time. This implies that the use of a SAO method is even more advantageous. Indeed, most approaches substantially reduced the computational cost, with a Speed-up of over 30 in most cases. The fastest approach was the 5-FCV, as it quickly converges while not being as costly as the LOOCV. However, the ASKIT clearly presented the lowest errors, since it reliably found results closer to the optimum design, as seen in Fig. 16. In addition, results suggest the ASKIT to be the most robust approach, considering that it seems to present the smallest deviation for the values of N_{cr} found. These aspects are in agreement to what was seen in previous examples.

7. Conclusion

This work presented different Sequential Approximate Optimization (SAO) procedures based on Radial Basis Functions (RBF) in order to lower the computational cost of the optimization process of functionally graded plates for eigenvalue problems. The buckling load and natural frequency are both approximated by a surrogate model,

Table 11
Metrics for Example 2 with smooth design constraint.

$\overline{V}_{c,max}$	SAO approach	Width	$\overline{n}_p$	$\overline{NRMSE}$	Speed-up
35%	EI	NAK	88	4.23%	13.47
		ASKIT	90	**1.01**%	11.82
		LOOCV	79	2.44%	6.86
		5-FCV	**74**	2.96%	**18.25**
	WEI	NAK	94	4.37%	11.26
		ASKIT	78	**1.60**%	16.02
		LOOCV	75	2.44%	8.19
		5-FCV	**74**	2.64%	**16.84**
50%	EI	NAK	107	4.72%	7.90
		ASKIT	83	**0.32**%	12.77
		LOOCV	73	1.15%	8.30
		5-FCV	**71**	1.20%	**15.92**
	WEI	NAK	77	5.39%	**14.33**
		ASKIT	81	**0.30**%	13.05
		LOOCV	83	1.35%	3.52
		5-FCV	**75**	1.07%	13.82
65%	EI	NAK	91	4.22%	10.09
		ASKIT	87	**0.39**%	11.32
		LOOCV	**74**	1.52%	6.53
		5-FCV	76	1.10%	**12.64**
	WEI	NAK	100	4.06%	9.90
		ASKIT	83	**0.47**%	13.15
		LOOCV	79	1.69%	5.76
		5-FCV	**68**	1.50%	**18.77**

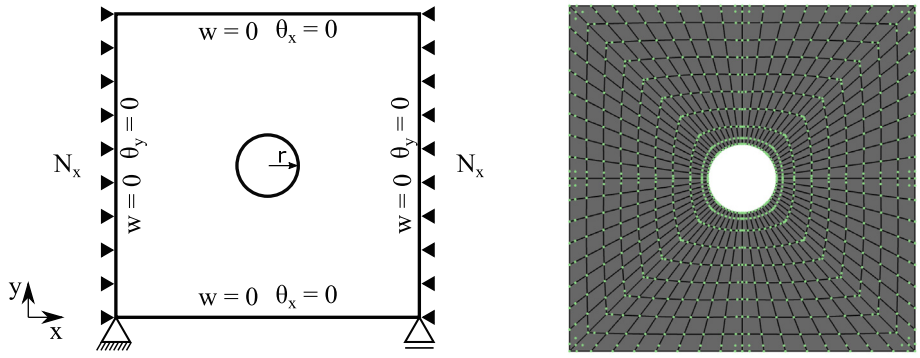

(a) Loading and boundary conditions (b) 16 × 16 cubic NURBS mesh

Fig. 14. Clamped FGM square plate with a hole.

Table 12
Optimal designs for Example 3.

Design variables	$\overline{V}_{c,max}$ = 35%		$\overline{V}_{c,max}$ = 50%		$\overline{V}_{c,max}$ = 65%	
	HFM	SAO	HFM	SAO	HFM	SAO
h (m)	0.0324	0.0324	0.0378	0.0378	0.0452	0.0452
$V_{c,1}$	1.0000	0.9985	1.0000	0.9995	0.9925	0.9937
$V_{c,2}$	1.0000	0.9995	1.0000	0.9987	0.9993	0.9956
$V_{c,3}$	0.3815	0.3556	1.0000	0.9978	0.9973	1.0000
$V_{c,4}$	0.0103	0.0010	0.0000	0.0008	0.4384	0.4495
$V_{c,5}$	0.0061	0.0605	0.0000	0.0023	0.0311	0.0069
N_{cr} ($\times 10^5$)	1.446	1.437	2.469	2.464	4.248	4.250
Difference		0.603%		0.187%		0.038%
$\overline{N}_{iter}$	121	51	107	45	111	43
$\overline{n}_p$	6050	81	5350	75	5550	73
Average time	7174 s	163 s	7576 s	158 s	6597 s	183 s

replacing the need for thousands of structural analyses based on high fidelity computational methods required by conventional optimization using heuristic algorithms.

A NURBS-based isogeometric formulation is used for structural analysis and a PSO algorithm is used for the maximization of the expected improvement and the objective function. The volume fraction distribution is defined using B-Splines and the design variables are the volume fraction at each control point, as well as the plate thickness in one of the examples. A new constraint limiting the variation of the ceramic volume fraction was included in the optimization model in

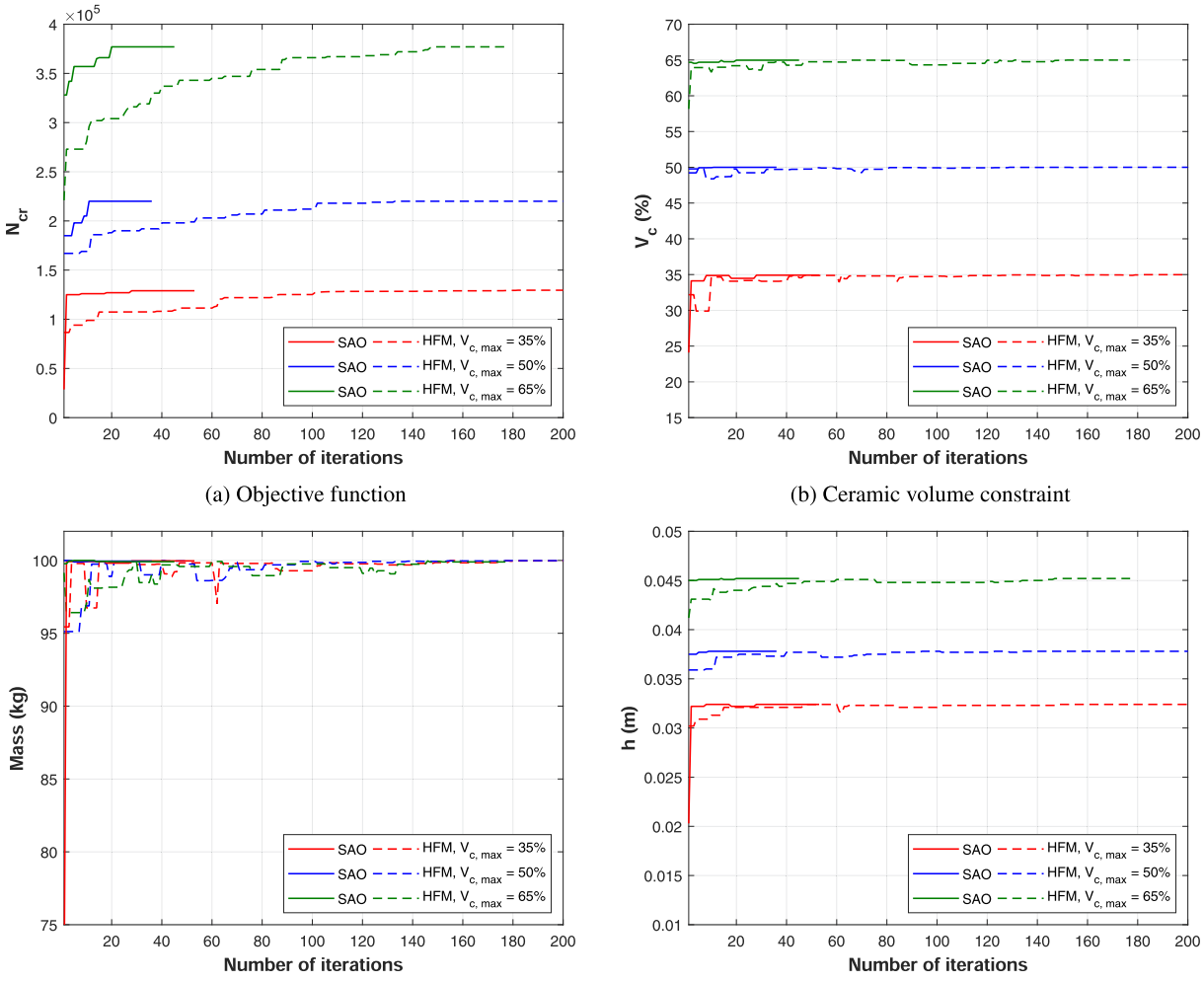

(a) Objective function

(b) Ceramic volume constraint

(c) Mass constraint

(d) Thickness

Fig. 15. Convergence history for Example 3.

Table 13
Metrics for Example 3 using the proposed SAO approaches.

$\overline{V}_{c,max}$	SAO approach	Width	$\overline{n}_p$	$\overline{NRMSE}$	Speed-up
35%	EI	NAK	92	4.44%	38.66
		ASKIT	75	**2.36%**	49.07
		LOOCV	**65**	3.11%	40.01
		5-FCV	73	4.45%	**51.84**
	WEI	NAK	85	4.07%	39.92
		ASKIT	81	**2.27%**	43.99
		LOOCV	**64**	4.07%	37.80
		5-FCV	**64**	3.99%	**44.70**
50%	EI	NAK	101	5.75%	26.68
		ASKIT	75	**0.61%**	40.84
		LOOCV	72	3.44%	20.06
		5-FCV	**63**	2.67%	**49.20**
	WEI	NAK	87	6.86%	26.12
		ASKIT	72	**0.93%**	44.35
		LOOCV	**64**	3.72%	28.80
		5-FCV	68	3.83%	**45.01**
65%	EI	NAK	88	4.63%	37.10
		ASKIT	71	**1.48%**	50.75
		LOOCV	64	2.30%	34.85
		5-FCV	**62**	3.60%	**54.52**
	WEI	NAK	93	4.87%	24.82
		ASKIT	73	**1.40%**	36.05
		LOOCV	67	3.26%	27.15
		5-FCV	**66**	3.52%	**49.12**

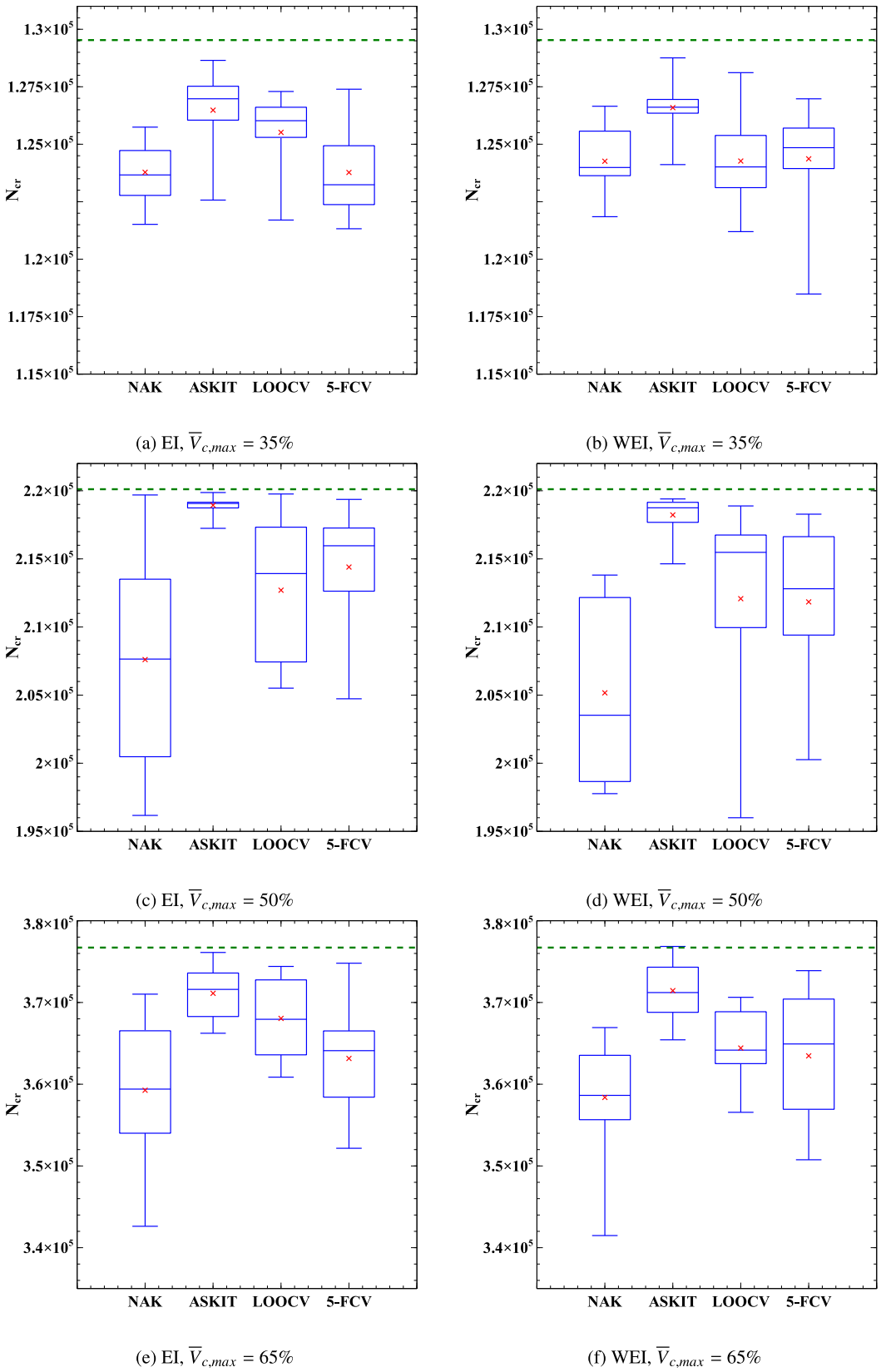

Fig. 16. Results on all approaches tested for Example 3.

order to successfully ensure a smooth design. Results showed that the importance of this constraint increases with the number of control points.

The results obtained using the SAO approaches were excellent, since they were able to significantly reduce the optimization time in all examples. Even in more complex problems, these approaches were

able to find results very close to the global optimum. The RBF, coupled with either conventional (EI) or weighted expected improvement (WEI) infill criteria was able to accurately predict both buckling load and natural frequency of functionally graded plates, using analytical or cross-validation methods to define the width parameter. Overall, the ASKIT method presented very good results in all cases, being the most accurate in the examples studied in this work. However, the 5-FCV method was the best in terms of efficiency, while presenting a good accuracy.

CRediT authorship contribution statement

Leonardo Gonçalves Ribeiro: Software, Formal analysis, Investigation, Data curation, Writing - original draft, Visualization. **Marina Alves Maia:** Software, Validation, Writing - review & editing. **Evandro Parente:** Conceptualization, Methodology, Software, Funding acquisition, Project administration, Writing - review & editing. **Antônio Macário Cartaxo de Melo:** Resources, Supervision, Writing - review & editing.

Declaration of Competing Interest

The authors declare that they have no known competing financial interests or personal relationships that could have appeared to influence the work reported in this paper.

Acknowledgements

This study was financed by the Conselho Nacional de Desenvolvimento Científico e Tecnológico (CNPq) and the Coordenação de Aperfeiçoamento de Pessoal de Nível Superior – Brasil (CAPES) - Finance Code 001. The authors gratefully acknowledge the financial support provided by these agencies.

References

[1] Shen HS. Functionally graded materials: nonlinear analysis of plates and shells. CRC Press; 2009.
[2] Kou X, Parks G, Tan S. Optimal design of functionally graded materials using a procedural model and particle swarm optimization. Comput-Aided Des 2012;44(4):300–10. https://doi.org/10.1016/j.cad.2011.10.007.
[3] Ashjari M, Khoshravan M. Mass optimization of functionally graded plate for mechanical loading in the presence of deflection and stress constraints. Compos Struct 2014;110:118–32. https://doi.org/10.1016/j.compstruct.2013.11.025.
[4] Shi J-X, Shimoda M. Interface shape optimization of designing functionally graded sandwich structures. Compos Struct 2015;125:88–95. https://doi.org/10.1016/j.compstruct.2015.01.045.
[5] Loja M, Barbosa J, Soares CM. Analysis of sandwich beam structures using kriging based higher order models. Compos Struct 2015;119:99–106. https://doi.org/10.1016/j.compstruct.2014.08.019.
[6] Kim NI, Hyunh TA, Lieu QX, Lee J. NURBS-based optimization of natural frequencies for bidirectional functionally graded beams. Arch Mech 2018;70(4):337–64.
[7] Truong TT, Nguyen-Thoi T, Lee J. Isogeometric size optimization of bi-directional functionally graded beams under static loads. Compos Struct 2019;227:111259. https://doi.org/10.1016/j.compstruct.2019.111259.
[8] Correia VMF, Madeira JA, Araújo AL, Soares CMM. Multiobjective optimization of ceramic-metal functionally graded plates using a higher order model. Compos Struct 2018;183:146–60. https://doi.org/10.1016/j.compstruct.2017.02.013.
[9] Correia VMF, Madeira JA, Araújo AL, Soares CMM. Multiobjective optimization of functionally graded material plates with thermo-mechanical loading. Compos Struct 2019;207:845–57. https://doi.org/10.1016/j.compstruct.2018.09.098.
[10] Lieu QX, Lee J, Lee D, Lee S, Kim D, Lee J. Shape and size optimization of functionally graded sandwich plates using isogeometric analysis and adaptive hybrid evolutionary firefly algorithm. Thin-Walled Struct 2018;124:588–604. https://doi.org/10.1016/j.tws.2017.11.054.
[11] Lieu QX, Lee J. An isogeometric multimesh design approach for size and shape optimization of multidirectional functionally graded plates. Comput Methods Appl Mech Eng 2019;343:407–37. https://doi.org/10.1016/j.cma.2018.08.017.
[12] Lieu QX, Lee J. A reliability-based optimization approach for material and thickness composition of multidirectional functionally graded plates. Compos Part B: Eng 2019;164:599–611. https://doi.org/10.1016/j.compositesb.2019.01.089.
[13] Wang C, Yu T, Curiel-Sosa JL, Xie N, Bui TQ. Adaptive chaotic particle swarm algorithm for isogeometric multi-objective size optimization of FG plates. Struct Multidiscip Optim 2019;60(2):757–78. https://doi.org/10.1007/s00158-019-02238-2.
[14] Huynh TA, Lieu XQ, Lee J. NURBS-based modeling of bidirectional functionally graded Timoshenko beams for free vibration problem. Compos Struct 2017;160:1178–90. https://doi.org/10.1016/j.compstruct.2016.10.076.
[15] Do D, Lee D, Lee J. Material optimization of functionally graded plates using deep neural network and modified symbiotic organisms search for eigenvalue problems. Compos Part B: Eng 2019;159:300–26. https://doi.org/10.1016/j.compositesb.2018.09.087.
[16] Rocha IBCM, Parente E, Melo AMC. A hybrid shared/distributed memory parallel genetic algorithm for optimization of laminate composites. Compos Struct 2014;107:288–97. https://doi.org/10.1016/j.compstruct.2013.07.049.
[17] Barroso ES, Parente E, Melo AMC. A hybrid PSO-GA algorithm for optimization of laminated composites. Struct Multidiscip Optim 2016;55(6):2111–30. https://doi.org/10.1007/s00158-016-1631-y.
[18] Forrester AIJ, Sobester A, Keane AJ. Engineering design via surrogate modelling: a practical guide. Wiley; 2008.
[19] Hussain MF, Barton RR, Joshi SB. Metamodeling: radial basis functions, versus polynomials. Eur J Oper Res 2002;138(1):142–54. https://doi.org/10.1016/s0377-2217(01)00076-5.
[20] Mehmani A, Chowdhury S, Meinrenken C, Messac A. Concurrent surrogate model selection (COSMOS): optimizing model type, kernel function, and hyper-parameters. Struct Multidiscip Optim 2017;57(3):1093–114. https://doi.org/10.1007/s00158-017-1797-y.
[21] Regis RG. Optimization of complex systems: theory, models, algorithms and applications. Adv Intell Syst Comput.https://doi.org/10.1007/978-3-030-21803-4..
[22] Nakayama H, Arakawa M, Sasaki R. Simulation-based optimization using computational intelligence. Optimiz Eng 2002;3(2):201–14. https://doi.org/10.1023/a:1020971504868.
[23] Garg S, Patra K, Pal SK, Chakraborty D. Effect of different basis functions on a radial basis function network in prediction of drill flank wear from motor current signals. Soft Comput 2007;12(8):777–87. https://doi.org/10.1007/s00500-007-0236-1.
[24] Kitayama S, Arakawa M, Yamazaki K. Sequential approximate optimization using radial basis function network for engineering optimization. Optim Eng 2010;12(4):535–57. https://doi.org/10.1007/s11081-010-9118-y.
[25] Kitayama S, Yamazaki K. Simple estimate of the width in Gaussian kernel with adaptive scaling technique. Appl Soft Comput 2011;11(8):4726–37. https://doi.org/10.1016/j.asoc.2011.07.011.
[26] Kitayama S, Huang S, Yamazaki K. Optimization of variable blank holder force trajectory for springback reduction via sequential approximate optimization with radial basis function network. Struct Multidiscip Optim 2012;47(2):289–300. https://doi.org/10.1007/s00158-012-0824-2.
[27] Kitayama S, Srirat J, Arakawa M, Yamazaki K. Sequential approximate multi-objective optimization using radial basis function network. Struct Multidiscip Optim 2013;48(3):501–15. https://doi.org/10.1007/s00158-013-0911-z.
[28] Li X, Gao W, Gu L, Gong C, Jing Z, Su H. A cooperative radial basis function method for variable-fidelity surrogate modeling. Struct Multidiscip Optim 2017;56(5):1077–92. https://doi.org/10.1007/s00158-017-1704-6.
[29] Yun W, Lu Z, Jiang X. An efficient reliability analysis method combining adaptive Kriging and modified importance sampling for small failure probability. Struct Multidiscip Optim 2018;58(4):1383–93. https://doi.org/10.1007/s00158-018-1975-6.
[30] Fan X, Wang P, Hao F. Reliability-based design optimization of crane bridges using Kriging-based surrogate models. Struct Multidiscip Optim 2019;59(3):993–1005. https://doi.org/10.1007/s00158-018-2183-0.
[31] Song X, Lv L, Sun W, Zhang J. A radial basis function-based multi-fidelity surrogate model: exploring correlation between high-fidelity and low-fidelity models. Struct Multidiscip Optim 2019;60(3):965–81. https://doi.org/10.1007/s00158-019-02248-0.
[32] Chen YT, Xiang S, Zhao WP. Generalized multiquadrics with optimal shape parameter and exponent for deflection and stress of functionally graded plates. Appl Mech Mater 2014;709:121–4. https://doi.org/10.4028/www.scientific.net/amm.709.121.
[33] Cheng YC, Jiang CP, Lin DH. Finite element based optimization design for a one-piece zirconia ceramic dental implant under dynamic loading and fatigue life validation. Struct Multidiscip Optim 2018;59(3):835–49. https://doi.org/10.1007/s00158-018-2104-2.
[34] Truong TT, Lee S, Lee J. An artificial neural network-differential evolution approach for optimization of bidirectional functionally graded beams. Compos Struct 2020;233:111517. https://doi.org/10.1016/j.compstruct.2019.111517.
[35] Wang GG, Shan S. Review of metamodeling techniques in support of engineering design optimization. J Mech Design 2007;129(4):370. https://doi.org/10.1115/1.2429697. ISSN 10500472.
[36] Jin R, Chen W, Simpson TW. Comparative studies of metamodelling techniques under multiple modelling criteria. Struct Multidiscip Optim 2001;23(1):1–13. https://doi.org/10.1007/s00158-001-0160-4. ISSN 1615147X.
[37] Diaz-Manriquez A, Toscano-Pulido G, Gomez-Flores W. On the selection of surrogate models in evolutionary optimization algorithms. In 2011 IEEE Congress of Evolutionary Computation (CEC).https://doi.org/10.1109/cec.2011.5949881..
[38] Gan N, Gu J. Hybrid meta-model-based design space exploration method for expensive problems. Struct Multidiscip Optim 2018;59(3):907–17. https://doi.org/10.1007/s00158-018-2109-x.
[39] Piegl LA, Tiller W. The NURBS book. Springer; 1997. ISBN 3540615458.

[40] Benveniste Y. A new approach to the application of Mori-Tanaka's theory in composite materials. Mech. Mater. 1987;6(2):147–57. https://doi.org/10.1016/0167-6636(87)90005-6.
[41] Medeiros MS, Jr., Parente E, Jr., Melo AMC. Influence of the micromechanics models and volume fraction distribution on the overall behavior of SiC/Al functionally graded pressurized cylinders. Latin Am J Solids Struct 16(4). https://doi.org/10.1590/1679-78255433..
[42] Mori T, Tanaka K. Average stress in matrix and average elastic energy of materials with misfitting inclusions. Acta Metall 1973;21(5):571–4. https://doi.org/10.1016/0001-6160(73)90064-3.
[43] Nikbakht S, Kamarian S, Shakeri M. A review on optimization of composite structures Part II: functionally graded materials. Compos Struct 2019;214:83–102. https://doi.org/10.1016/j.compstruct.2019.01.105.
[44] Reddy JN. Mechanics of laminated composite plates and shells: theory and analysis. CRC Press; 2004. ISBN 9780849315923.
[45] Praciano JSC, Barros PSB, Barroso ES, Parente E, Holanda AS, Sousa JBM. An isogeometric formulation for stability analysis of laminated plates and shallow shells. Thin-Walled Struct 2019;143. https://doi.org/10.1016/j.tws.2019.106224. 106224.
[46] Auad SP, Praciano JSC, Barroso ES, Sousa JBM, Parente E. Isogeometric analysis of FGM plates. Mater Today: Proc 2019;8:738–46. https://doi.org/10.1016/j.matpr.2019.02.015.
[47] Kennedy J, Eberhart R. Particle swarm optimization. vol. 4; 1995..
[48] Bratton D, Kennedy J. Defining a standard for particle swarm optimization. In 2007 IEEE Swarm Intelligence Symposium.https://doi.org/10.1109/SIS.2007.368035..
[49] Michalewicz Z, Schoenauer M. Evolutionary algorithms for constrained parameter optimization problems. Evol Comput 1996;4(1):1–32. https://doi.org/10.1162/evco.1996.4.1.1.
[50] Steponavičė I, Shirazi-Manesh M, Hyndman RJ, Smith-Miles K, Villanova L. On sampling methods for costly multi-objective black-box optimization. In: Advances in stochastic and deterministic global optimization Springer optimization and its applications. p. 273–96. https://doi.org/10.1007/978-3-319-29975-4_15.
[51] Amouzgar K, Strömberg N. Radial basis functions as surrogate models with a priori bias in comparison with a posteriori bias. Struct Multidiscip Optim 2017;55(4):1453–69. https://doi.org/10.1007/s00158-016-1569-0.
[52] Goel T, Haftka RT, Shyy W, Queipo NV. Ensemble of surrogates; 2006..
[53] Hardy RL. Multiquadric equations of topography and other irregular surfaces. J Geophys Res 1971;76(8):1905–15. https://doi.org/10.1029/jb076i008p01905.
[54] Haykin S. Neural networks: a comprehensive foundation. Macmillan Publishing; 1994.
[55] Muller J, Shoemaker CA. Influence of ensemble surrogate models and sampling strategy on the solution quality of algorithms for computationally expensive black-box global optimization problems. J Global Optim 60(2); 2014: 123-144. https://doi.org/10.1007/s10898-014-0184-0..
[56] Sobester A, Leary SJ, Keane AJ. On the design of optimization strategies based on global response surface approximation models. J Global Optim 2005:31–59. https://doi.org/10.1007/s10898-004-6733-1.
[57] Elisseeff A, Pontil M. Leave-one-out error and stability of learning algorithms with applications Stability of Randomized Learning Algorithms Source. Int J Syst Sci 6..
[58] Schmit L, Farshi B. Some approximation concepts for structural synthesis. AIAA J 1974;12(5):692–9. https://doi.org/10.2514/3.49321.
[59] Khalfallah S, Ghenaiet A. Radial basis function-based shape optimization of centrifugal impeller using sequential sampling. Proc Inst Mech Eng Part G 229(4), 2014,:648–65. https://doi.org/10.1177/0954410014538421.
[60] Jones DR, Schonlau M, Welch WJ. Efficient global optimization of expensive black-box functions. J Global Optim 1998:455–92. https://doi.org/10.1023/A:100830643.
[61] Xiang H, Li Y, Liao H, Li C. An adaptive surrogate model based on support vector regression and its application to the optimization of railway wind barriers. Struct Multidiscip Optim 2016;55(2):701–13. https://doi.org/10.1007/s00158-016-1528-9.
[62] Bateni M, Kiani Y, Eslami M. A comprehensive study on stability of FGM plates. Int J Mech Sci 2013;75:134–44. https://doi.org/10.1016/j.ijmecsci.2013.05.014.
[63] Nguyen N-T, Hui D, Lee J, Nguyen-Xuan H. An efficient computational approach for size-dependent analysis of functionally graded nanoplates. Comput Methods Appl Mech Eng 2015;297:191–218. https://doi.org/10.1016/j.cma.2015.07.021.